

Mode Penetration Induced By Transient Magnetic Perturbations

M. T. Beidler, J. D. Callen, C. C. Hegna, and C. R. Sovinec

*Department of Engineering Physics, University of Wisconsin, Madison, WI 53706, USA**

Three dimensional magnetic fields in tokamaks can induce forced magnetic reconnection (FMR) and produce magnetic islands on resonant surfaces. Conventional analytic solutions to FMR focus on describing the time asymptotic state given a steady-state field error. The focus of this work is to understand the nonlinear dynamics of mode penetration, an evolution from a high-slip, flow-screened metastable equilibrium into a low-slip, field-penetrated metastable equilibrium. In this work, we extend previous work by incorporating a temporally varying external magnetic field as a simple model for an MHD event that produces resonant magnetic perturbations. Proof-of-principle, extended-MHD, NIMROD computations vary parameterizations of the transient external perturbation to probe the threshold for mode penetration. We test these computational results against analytical theory that captures the temporal evolution properties of the electromagnetic and viscous forces during and after a transient. We find qualitative agreement between computational and analytical results. However, computational tools are necessary to accurately capture the threshold conditions for mode penetration induced by an MHD transient.

I. INTRODUCTION

Unstable ideal and resistive magnetohydrodynamic (MHD) events in tokamaks transiently perturb the axisymmetric magnetic configuration. Resonant components of the magnetic fields associated with these events can drive forced magnetic reconnection (FMR) on resonant surfaces. Transient resonant magnetic perturbations can play a prominent role in seeding neoclassical tearing modes (NTMs) from their benign metastable equilibrium (*e.g.* Ref. [1] and references therein), and prompting the transition to a state of ELM suppression [2, 3] or mitigation. As both NTMs and ELMs have unfavorable consequences for tokamak operation, understanding how transient MHD events affect these phenomena is critical to encourage the success of ITER. In this paper, we extend prior calculations [4] by including a transient resonant magnetic perturbation source in extended-MHD calculations of forced magnetic reconnection of a flowing plasma.

It is observed that a large fraction of tokamak discharges disrupt due to NTM-induced locked modes [5]. Often, sawteeth or ELMs that directly precede the nonlinear growth of NTMs may provide a resonant magnetic perturbation that seeds island growth [1]. In addition to seeding NTMs, ELMs are also undesirable due to the effects they have on tokamak walls [6, 7]. Fortunately, the application of externally-applied three dimensional (3D) resonant magnetic perturbations (RMPs) may help mitigate and even avoid ELMs [8–11]. Additionally, recent experiments on DIII-D ramped the magnitude of RMP fields slowly [2, 3], allowing the observation of the conditions directly before the transition to an ELM suppressed state. Naturally, there is always a final ELM before an ELM suppressed state is reached. A detailed analysis immediately following the final ELM shows that it supplies a magnetic perturbation that induces a locked island at the top of the pedestal. This prevents the expansion of the width of the steep gradient region of the pedestal

so that edge peeling-ballooning modes are avoided and allows entry into the ELM suppressed state [12].

A central issue in understanding both processes is understanding how transient magnetic perturbations affect FMR processes on resonant surfaces in a tokamak. The time-dependent details of FMR have been studied without [13] and with flow [14]. However, the majority of the FMR studies for tokamak applications to non-axisymmetric fields have focused on the time-asymptotic state [15–38].

In particular, Ref. [15] introduced the concept of mode penetration, whereby an initially flow-screened external field abruptly penetrates, making a transition to a nonlinear island state. The details of this process involves the coupled evolution of the field and flow response at the rational surface. While many properties of mode penetration can be understood from the time-asymptotic theory, a full understanding of the nonlinear dynamics requires a more detailed analysis. Compared to the many studies of FMR focusing on the time-asymptotic state, relatively few numerical studies [4, 39, 40] investigate the physics of nonlinear mode penetration due to RMPs.

Additional research has explored the time-dependent formation of seed islands for NTMs analytically [41] and experimentally [42, 43]. While the aforementioned studies have examined the separate physics of time-dependent, FMR due to transient RMPs in a flowing plasma, these elements have not yet been combined in one comprehensive theory. Furthermore, the time-dependent studies mentioned above are initialized from a state with no penetrated field, while experimental observations suggest that NTMs and ELM suppressed states begin from a metastable equilibrium with small initial magnetic islands.

In this paper, we examine the effects of a transient MHD perturbation on FMR in a slab geometry, employing computational and analytical methods. Computational investigations employ the nonlinear, extended-MHD code NIMROD [44], and analytical investigations extend the results of Ref. [15] to include time-dependent electromagnetic (EM) and viscous forces. The remainder of the paper is organized as follows. Section II describes the computational methods and initialization employed

* Emails to: beidler@wisc.edu

in the NIMROD code. Section III gives a brief review of the time-asymptotic, quasilinear force-balance needed to initialize a metastable equilibrium when a RMP is present [4, 15]. Section IV presents nonlinear computational results of the stimulation of mode penetration by the addition of a transient magnetic perturbation, including a parametric study of the transient to probe the threshold for mode penetration. In section V we extend the analytics of Ref. [15] by generalizing the EM and viscous forces to allow for changing externally-applied field and the resulting flow profiles, and then compare these analytical predictions to computational results. Details of the analytic modeling used in this section are provided in Appendices A and B. A section containing conclusions and discussion closes the paper.

II. NUMERICAL METHODS AND INITIALIZATION

A. The NIMROD Code

The computational methods and initialization are largely the same as that in Ref. [4]. A summary of the details are presented here for completeness. The NIMROD code [44] solves the nonlinear, extended-MHD equations. Here, we use NIMROD to solve the visco-resistive MHD equations given by:

$$\rho \left(\frac{\partial \mathbf{V}}{\partial t} + \mathbf{V} \cdot \nabla \mathbf{V} \right) = \mathbf{J} \times \mathbf{B} - \nabla \cdot \mathbf{\Pi}_i, \quad (1a)$$

$$\frac{\partial \mathbf{B}}{\partial t} = -\nabla \times \mathbf{E} + \kappa_{divbd} \nabla \nabla \cdot \mathbf{B}, \quad (1b)$$

$$\mathbf{E} = -\mathbf{V} \times \mathbf{B} + \eta \mathbf{J}, \quad (1c)$$

$$\mu_0 \mathbf{J} = \nabla \times \mathbf{B}. \quad (1d)$$

The single-fluid velocity \mathbf{V} , and magnetic field \mathbf{B} are evolved in time using a time-centered, semi-implicit leapfrog algorithm, which allows use of time steps exceeding the CFL condition. Equation (1a) describes the evolution of the single-fluid velocity with mass density $\rho = nM_i$, with the spatially constant particle density n held constant in time. Equation (1b) is Faraday's law for the evolution of the magnetic field. Equation (1c) is the resistive-MHD Ohm's law, where η is the electrical resistivity and \mathbf{J} is the current density. Equation (1d) is Ampère's law for current density. The quantity κ_{divbd} is introduced to control numerical divergence error [44]. The dissipation parameter ν in $\mathbf{\Pi}_i \equiv -\rho\nu[\nabla \mathbf{V} + \nabla \mathbf{V}^T - (2/3)\nabla \cdot \mathbf{V}]$ within Eq. (1a) describes the isotropic viscosity, in which $\nabla \mathbf{V}^T$ is the transpose of $\nabla \mathbf{V}$. We note that we are computing a cold plasma in this study, by setting $\beta \equiv p/(B^2/2\mu_0) = 0$.

Computations use the semi-implicit methods described in [44, 45], where the equilibrium fields are held constant and perturbation fields are evolved. NIMROD is a 3D code that is used to solve the system of equations (1a-d) in 2D. Perturbation fields are numerically represented by employing two-dimensional spectral elements of arbitrary polynomial degree along with a truncated Fourier series representation in the third dimension. Because the

present study focuses on details in the 2D plane, only the $n = 0$ harmonic of the Fourier representation is used.

Physical quantities appearing hereafter are in their dimensionless form. Their normalizations are derived from a characteristic length, density, and magnetic field of $L_{\text{norm}} = 1$ m, $n_{\text{norm}} = 10^{19}$ particles m^{-3} , and $B_{\text{norm}} = 0.1$ T. This sets the normalization for velocity to $V_{\text{norm}} \equiv c_A = B_{\text{norm}}/(\mu_0 n_{\text{norm}} M_i)^{1/2} = 6.90 \times 10^5$ m/s, which is the Alfvén speed based on the characteristic magnetic field and density for hydrogen, and the time to $t_{\text{norm}} \equiv \tau_A = L_{\text{norm}}/V_{\text{norm}} = 1.45 \times 10^{-6}$ s, the characteristic Alfvén time. The normalization used for the dissipation parameters κ_{divbd} , ν , and η/μ_0 is $D_{\text{norm}} = L_{\text{norm}}^2/t_{\text{norm}} = 6.90 \times 10^5$ m^2/s .

B. Initialization and Optimization

All computations are run with a domain having dimensions $(L_x, L_y) = (2, 2) L_{\text{norm}}$, so that $k_y \equiv 2n\pi/L_y = n\pi L_{\text{norm}}^{-1}$. We use a representation with 96×48 quartic elements in the x, y plane. We also employ mesh packing along the x direction at $|x| = 0$ and $a \equiv L_x/2 = L_{\text{norm}}$, where the minimum grid spacing is approximately $7.5 \times 10^{-3} L_{\text{norm}}$. We have run additional computations to verify that this resolution is sufficient to resolve the dominant physical mechanisms under examination in this study.

We initialize the computations in accordance with Taylor's problem [13]. The force-free equilibrium magnetic field has components in the y and z directions, which has a linearly-sheared profile of B_y in the x direction, and an out-of-plane component in the z direction. Note that equilibrium quantities are denoted by subscript 0. The magnetic field profile for this equilibrium $\mu_0 \mathbf{J}_0 = \lambda \mathbf{B}_0$ is generated by setting the out-of-plane field at $x = 0$ to $B_{z,0} = 100 B_{\text{norm}}$, the in-plane field normal to the resonant surface throughout the computational domain to $B_{x,0} = 0$, and numerically integrating the chosen parallel current profile

$$\lambda \equiv \frac{\mu_0 \mathbf{J}_0 \cdot \mathbf{B}_0}{B_0^2} = \frac{\lambda_0}{a} \text{sech}^2 \left(\frac{\lambda_0 x}{a} \right), \quad (2)$$

with $\lambda_0 = 0.01$. This yields a nearly linear profile of $B_{y,0}(x)$ with $B_{y,0}(x = \pm a) = \pm 1 B_{\text{norm}}$. This magnetic profile with $k_{y,n=1} a = \pi$ has a tearing stability index $a\Delta'_0 \equiv -2k_y a / \tanh(k_y a) \simeq -2\pi$ [4, 46], whose negative value implies stability [47]. The global Alfvén time τ_A , cited in the previous section, is based on a and B_{norm} , which is the in-plane component of \mathbf{B} at the boundary.

The equilibrium flow profile $V_{y,0}(x)$ has the form of a Gaussian with half-width equal to $0.25 a$, which nears zero at $|x| = a$ and is relatively flat at the resonant surface with $V_{y,0}(0) = 7.25 \times 10^{-4} c_A$. This profile is chosen in order to suppress any unintended effects from flow shear at the resonant surface while satisfying no-slip boundary conditions. Implied sources keep these equilibrium profiles of current and plasma flow constant, as only perturbation fields are being evolved by NIMROD [44, 45].

Prescribed resistive and viscous diffusion parameters set the dissipation layer width and reconnection time scales. The resistivity used throughout all computations is set to $\eta/\mu_0 = 2.90 \times 10^{-7} D_{\text{norm}}$, resulting in a global Lundquist number $S \equiv \tau_R/\tau_A = 3.45 \times 10^6$, where $\tau_R \equiv a^2/(\eta/\mu_0) = 3.45 \times 10^6 \tau_A$ is the resistive diffusion time based on the half-length of the x direction. The prescribed isotropic viscosity has a profile given by $\nu_0 \bar{\nu}(x) \equiv \nu_0 [1 + (\Delta_{\text{mag}}^{1/2} - 1) \times (|x|/a)^{\Delta_{\text{width}}}]^2$, which is consistent with a flat profile at $x = 0$ and edge regions at $|x| \sim a$. All computations use $\Delta_{\text{mag}} = 1000$ and $\Delta_{\text{width}} = 5$, which yield an edge region that falls to $\sim \nu_0$ at $|x| \sim a/2$. This additional diffusion avoids unresolved boundary layers while not qualitatively affecting the results, as additional computations have shown. The value of the isotropic viscosity coefficient is set to $\nu_0 = 5.80 \times 10^{-6} D_{\text{norm}}$, which results in a value for the magnetic Prandtl number $P_m \equiv \tau_R/\tau_\mu = 20$, where $\tau_\mu \equiv a^2/\nu_0 = 1.72 \times 10^5 \tau_A$ is the viscous diffusion time based on the half-length of the x direction.

With this flow and dissipation, the system corresponds to the visco-resistive (VR) regime of Ref. [16], which is expected to be important for tokamak physics [15]. In the VR regime, the dissipation layer width is given by $\delta_{\text{VR}} = a S_{\text{sh}}^{-1/3} P_m^{1/6} = 7.45 \times 10^{-3} L_{\text{norm}}$, and the dissipation layer time is given by $\tau_{\text{VR}} = 2.104 \tau_{\text{shA}} S_{\text{sh}}^{2/3} P_m^{1/6} = 5.4 \times 10^4 \tau_A$. Here, $\tau_{\text{shA}} \equiv \tau_A/k_y a$ is the shear Alfvén time (called the local hydromagnetic time scale in Ref. [15]) and $S_{\text{sh}} \equiv S k_y a$ is the shear Alfvén Lundquist number.

With the characteristic Alfvén time in mind, we choose a fixed time step of $dt = 0.689 \tau_A$ at which to evolve the computations to avoid ill-conditioned matrices when solving the implicit systems. We have also run computations with a lower time step, and only found slight quantitative differences in the system’s evolution. With this fixed time step, we have run multiple computations varying κ_{divbd} and find that a value of $\kappa_{\text{divbd}} = 7.25 \times 10^{-5} D_{\text{norm}}$ is large enough to control the numerical divergence error with the spatial representation described above.

The equilibrium is perturbed by a spatially non-uniform edge magnetic field, which has in-plane components normal (\hat{x}) and tangential (\hat{y}) to the resonant surface at $x = 0$. The value of the normal, “applied field” at the $|x| = a$ boundary is prescribed to evolve in time as $B_{\text{ext}}(t)$. The evolution of $B_{\text{ext}}(t)$ is consistent with an applied, nonuniform, tangential electric field being applied at the boundary $E_{\text{ext}}(t)$, according to Faraday’s law $\hat{y} \cdot [\partial \mathbf{B}/\partial t = -\nabla \times \mathbf{E}]$. Because this tangential electric field will induce a tangential magnetic field within the plasma, we explicitly impose the time evolution of the normal magnetic and tangential electric fields at $|x| = a$ and allow the tangential magnetic field to self-consistently evolve in the computed plasma region.

Computations are initialized with boundary fields hav-

ing spatial and time dependence parameterized by

$$B_{\text{ext}}(y, t) = B_{\text{ext},0} \sin(k_y y) T_{\text{NIM}}(t), \quad (3a)$$

$$E_{\text{ext}}(y, t) = \frac{B_{\text{ext},0}}{k_y} \cos(k_y y) \frac{dT_{\text{NIM}}(t)}{dt}, \quad (3b)$$

$$T_{\text{NIM}}(t, \tau_0) = 1 - e^{-t/\tau_0} - \frac{t}{\tau_0} e^{-t/\tau_0}. \quad (3c)$$

The time-dependence is the same as that employed by Refs. [46, 48, 49] for a boundary displacement consistent with Ref. [13]. For perspective on this form of the time-dependence, we note that $T_{\text{NIM}} \simeq 0.96$ at $t = 5 \tau_0$. All computations are initialized with $\tau_0 = 69.0 \tau_A$, which is significantly larger than τ_A .

III. ANALYTICS OF TIME-ASYMPTOTIC FORCE BALANCE

In this section, we review the quasilinear model developed in Ref. [4], which was adapted from the cylindrical geometry model of Ref. [15] for slab geometry.

We are concerned with the time-asymptotic force balance at the resonant surface, between the two terms on the right-hand side (RHS) of Eq. (1a), the EM and viscous force densities

$$\mathbf{F}_{\text{EM}} = \mathbf{J} \times \mathbf{B}, \quad (4a)$$

$$\mathbf{F}_{\text{V}} = -\nabla \cdot \Pi_i \simeq \nabla \cdot \rho \nu \nabla \mathbf{V}. \quad (4b)$$

For the case of a static applied magnetic field with plasma flowing at the resonant surface, the EM force generates a force on the plasma producing a local flow opposite to that of the equilibrium flow. The altered flow profile generates a viscous force that balances the EM force. The EM force is a strong function of the self-consistently generated flow at the resonant surface. Thus, the nonlinear time-asymptotic state depends on the self-consistent flow response to the applied field.

In order to ascertain the effects of the time-asymptotic force balance, we integrate the force densities over the y dimension and across the dissipative layer at the resonant surface, of width δ_{VR} , where non-ideal physics allows eddy currents to be driven that contribute to an EM force on the plasma. These integrations yield $\hat{\mathbf{F}}$, the force per unit length in the symmetry direction z , according to

$$\hat{\mathbf{F}} \equiv \int_{-\delta_{\text{VR}}/2}^{\delta_{\text{VR}}/2} dx \int_{-L_y/2}^{L_y/2} dy \mathbf{F}. \quad (5)$$

We only consider the \hat{y} -component of $\hat{\mathbf{F}}$ (*i.e.*, $\hat{y} \cdot \hat{\mathbf{F}}$), because only flows parallel to the spatial modulation in the applied field (*i.e.* $\mathbf{k} \cdot \mathbf{V} \neq 0$) produce eddy currents that generate forces at the resonant surface. General forms of EM and viscous forces per unit length are given in

Appendices A and B, respectively, of Ref. [4] as

$$\hat{F}_{y,\text{EM}} = -\frac{L_y}{2\mu_0 k_y} \mathcal{I}m \left\{ B_x^* \frac{\partial B_x}{\partial x} \right\} \Bigg|_{-\delta_{\text{VR}/2}}^{\delta_{\text{VR}/2}} \simeq -\frac{L_y}{2\mu_0 k_y} \Delta'_{\text{ext}} B_{\text{ext}} \mathcal{I}m \{ B_{\text{res}}^* \}, \quad (6a)$$

$$\hat{F}_{y,\text{V}} = L_y \rho \nu_0 \left[\frac{\partial V_y}{\partial x} \right]_{-\delta_{\text{VR}/2}}^{\delta_{\text{VR}/2}}, \quad (6b)$$

where $B_{\text{res}} \equiv B_x(x=0)$ is the field response at the resonant surface, * indicates a complex-conjugate, and $a\Delta'_{\text{ext}} = 2k_y a / \sinh(k_y a) \simeq 0.54$ is the tearing drive due to the external field [4, 46]. We note that Appendix A in Ref. [4] represents the field response using a Fourier expansion with complex coefficients. Thus, B_x and B_{res} in Eq. (6a) are complex-valued and contain information on the magnitude and relative phase of the field response, with $\mathcal{R}e\{B_x\} = (B_x + B_x^*)/2$.

The response at $x=0$ of a field $B_{\text{ext}} \sin(k_y y)$ applied at $|x|=a$ is governed by Eqs. (1a-d). The time-independent solution is provided by the linear analytics of Ref. [15], which yields

$$B_{\text{res}} = \frac{a\Delta'_{\text{ext}}}{-a\Delta'_0 + i\omega_{\text{res}}\tau_{\text{VR}}} B_{\text{ext}}, \quad (7)$$

where $\omega_{\text{res}} = \mathbf{k} \cdot \mathbf{V}(x=0)$ is the flow frequency at $x=0$ and we are in the VR regime. The contribution in Eq. (7) proportional to the $i\omega_{\text{res}}\tau_{\text{VR}}$ denotes the plasma response to the applied field due to the plasma rotation. Assuming that the asymmetric $k_y \neq 0$ equilibrium responses are described by the linear analytics, Eq. (6a) is given by

$$\hat{F}_{y,\text{EM}} = -\frac{\omega_{\text{res}}\tau_{\text{VR}}}{(-a\Delta'_0)^2 + (\omega_{\text{res}}\tau_{\text{VR}})^2} \frac{L_y (a\Delta'_{\text{ext}})^2 B_{\text{ext}}^2}{2ak_y \mu_0}. \quad (8)$$

We note that this is a net force density on the plasma due to the $k_y \neq 0$, quasilinear, quadratic, $\mathbf{J} \times \mathbf{B}$ response.

In order to calculate the viscous force according to Eq. (6b), the jump in the flow profile at the rational surface must be determined. Because the EM force is only nonzero near the resonant surface, in the time-asymptotic state Eq. (1a) reduces to

$$\frac{\partial}{\partial x} \left[\bar{\nu}(x) \frac{\partial V_y(x,t)}{\partial x} \right] = 0, \quad (9)$$

in the region $0 \lesssim |x| < a$, which can be solved for the flow profile. The time-independent solution is worked out in appendix B of Ref. [4], yielding their Eqs. (B4) and (B6). An inspection of those equations demonstrates the time-asymptotic flow profile is approximately $V_y(x) \simeq V_y(0) + [V_{y,0} - V_y(0)](x/a_\nu)$, where $a_\nu \equiv \int_0^a dx' / \bar{\nu}(x')$. The effect of the viscosity profile $\bar{\nu}(x)$ is essentially to move the no-slip boundary condition from $x=a$ to $x=a_\nu$. In the region $0 < |x| < a_\nu$, viscosity is approximately constant at ν_0 .

Using the time-asymptotic flow profile in Eq. (6b), the net viscous force density yields

$$\hat{F}_{y,\text{V}} = \frac{2L_y \rho \nu_0}{k_y a_\nu} (\omega_0 - \omega_{\text{res}}), \quad (10)$$

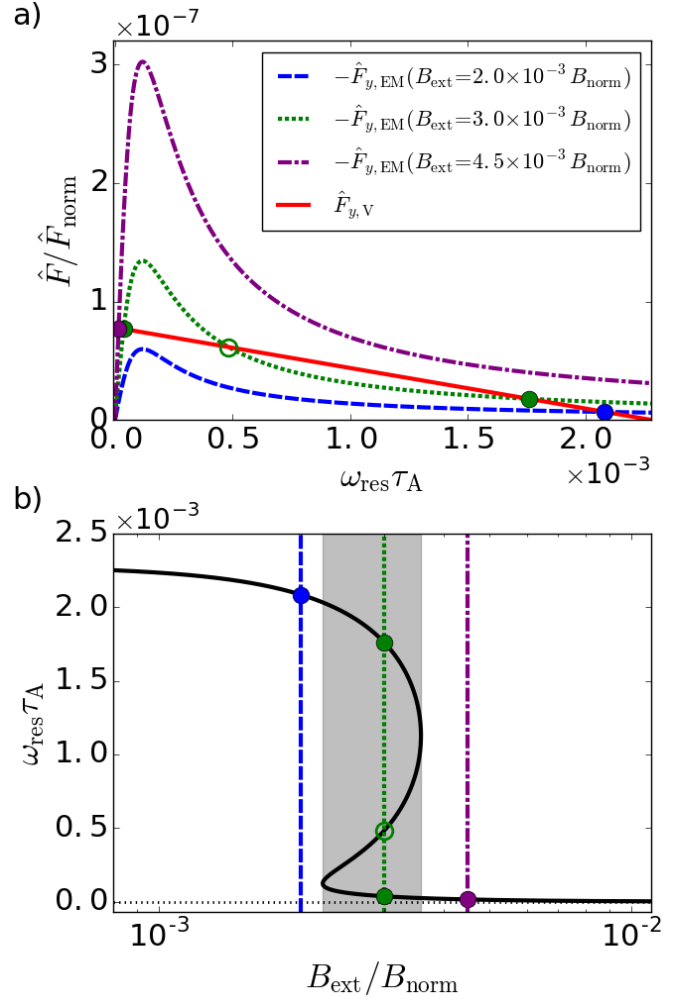


FIG. 1. a) Analytically calculated quasilinear electromagnetic and viscous forces, according to Eqs. (8) and (10), respectively. The dashed (blue), dotted (green), and dashed-dotted (purple) traces correspond to $\hat{F}_{y,\text{EM}}$ solutions with increasing externally applied magnetic field B_{ext} , where the solid (red) trace corresponds to $\hat{F}_{y,\text{V}}$. Filled circles correspond to stable or metastable equilibria, while the open circle corresponds to an unstable equilibrium. b) Time-asymptotic force balance for the $\hat{F}_{y,\text{EM}}$ and $\hat{F}_{y,\text{V}}$ in a). The solid (black) trace corresponds to equilibria according to Eq. (11), and the grey region indicates a metastable region with two metastable equilibria at a single B_{ext} .

where $\omega_0 = \mathbf{k} \cdot \mathbf{V}_0$ is the flow frequency as determined by the imposed equilibrium flow. The viscous force is linearly proportional to the shift in the bulk flow away from its initial value and consistent with the form of the viscous force given in [4]. Again, the following NIMROD calculations use $\Delta_{\text{mag}} = 1000$ and $\Delta_{\text{width}} = 5$ to yield $a_\nu/a = 0.431$.

Figure 1 shows analytically calculated forces as a function of ω_{res} for the equilibrium and dissipation parameters defined in Section II B. These parameters are used throughout the rest of this paper. Figure 1a shows dash-dotted (purple), dotted (green), and dashed (blue) traces corresponding to the negative of the time-asymptotic EM force per unit length given in Eq. (8) for different mag-

nitudes of B_{ext} . The force per unit length is normalized to $\hat{F}_{\text{norm}} \equiv B_{\text{norm}}^2/2\mu_0 = 3.98 \times 10^3 \text{ N/m}$. The solid (red) trace corresponds to the time-independent viscous force given in Eq. (10), and equilibria are marked with circles where the EM and viscous forces balance. The equilibria can be stable or metastable (solid circles), or unstable (open circle), as is apparent from the net force in the vicinity of each equilibrium. The dashed curve has the smallest external forcing, resulting in a large ω_{res} (high-slip) equilibrium, that is flow-screened consistent with Eq. (7). In this case, the applied field is too weak to greatly alter the flow velocity and large screening currents persist and prevent the applied field from penetrating to the rational surface. Conversely, for the dash-dotted curve with the largest external forcing, the resulting equilibrium is at small ω_{res} (low-slip), and the external field penetrates to the resonant surface. For the intermediate external forcing represented by the dotted line, both flow-screened and field-penetrated metastable equilibria exist, in addition to an unstable equilibrium.

Next, balancing these two time-asymptotic, forces per unit length according to $\hat{F}_{y,\text{EM}} + \hat{F}_{y,\text{V}} = 0$, results in the relation

$$\frac{\omega_0}{\omega_{\text{res}}} - 1 + \omega_0 \omega_{\text{res}} \tau_{\text{VR}}'^2 - \omega_{\text{res}}^2 \tau_{\text{VR}}'^2 = \frac{a_{\nu} \tau_{\text{VR}}}{4a\nu_0} \left(\frac{\Delta'_{\text{ext}}}{-\Delta'_0} \right)^2 \frac{B_{\text{ext}}^2}{\mu_0 \rho} \equiv A_{\text{T}} \left(\frac{B_{\text{ext}}}{B_{0,z}} \right)^2, \quad (11)$$

where $\tau_{\text{VR}}' = \tau_{\text{VR}}/(-a\Delta'_0) = 8.59 \times 10^3 \tau_{\text{A}}$. The solution of this cubic equation for ω_{res} is shown by the solid (black) line in Fig. 1b. Vertical lines plotted in Fig. 1b correspond to the curves of different external forcing in Fig. 1a. Reference [4] showed that nonlinear computations with the NIMROD code reproduced time-asymptotic equilibria consistent with this analytic prediction. After initialization of the external perturbation described by Eq. (3a), the computation is extended out until ω_{res} changes by $\lesssim 0.1\%$ over $\sim 10^4 \tau_{\text{A}}$. We find initial time-asymptotic equilibria are within $\sim 1\%$ of the analytic predictions for ω_{res} .

Analytically, the solution to Eq. (11) exhibits multiple solutions when the initial flow frequency ω_0 is above a critical threshold [15] given by

$$\omega_0 > \omega_{0,\text{crit}} = \frac{3\sqrt{3}}{\tau_{\text{VR}}'}. \quad (12)$$

For the parameters used in this study, $\omega_0 \tau_{\text{VR}}' \simeq 19.5$, which corresponds to the wide metastable region indicated by the shaded region in Fig. 1b. Note that $\omega_{0,\text{crit}}$ only depends on τ_{shA} , S_{sh} , P_{m} , and Δ'_0 ; thus the initial flow frequency at which a bifurcation can occur is independent of the applied field B_{ext} .

The RMP amplitudes B_{ext} where the metastable states occur can be estimated by examining Eq. (11), assuming $\omega_0 \tau_{\text{VR}}' \gg 1$ and finding where the left hand side (LHS) satisfies $d\text{LHS}/d\omega_{\text{res}} = 0$. The minimum B_{ext} for the metastable state occurs at $\omega_{\text{res}} \simeq 1/\tau_{\text{VR}}'$, which yields

$$B_{\text{ext},\text{min}} \simeq B_{0,z} \sqrt{2\omega_0 \tau_{\text{VR}}'/A_{\text{T}}} \simeq 2.3 \times 10^{-3} B_{\text{norm}}, \quad (13)$$

using $A_{\text{T}} = 7.4 \times 10^{10}$ for the parameters of this study. The maximum B_{ext} of the metastable state occurs at $\omega_{\text{res}} \simeq \omega_0/2$, which yields

$$B_{\text{ext},\text{max}} \simeq B_{0,z} \omega_0 \tau_{\text{VR}}' / (2\sqrt{A_{\text{T}}}) \simeq 3.6 \times 10^{-3} B_{\text{norm}}. \quad (14)$$

Numerical values at the ends of Eqs. (13) and (14) agree with NIMROD results shown in Fig. 1b. The result in Eq. (14) agrees with the definition of $B_{\text{ext},\text{pen}}$ in Eq. (22) of Ref. [4] for $\omega_0 \tau_{\text{VR}}' \gg 1$. Thus, beyond the upper limit for the metastable state, complete penetration of B_{ext} always occurs. The approximate ratio of the maximum to minimum field for metastable behavior is $B_{\text{ext},\text{max}}/B_{\text{ext},\text{min}} \simeq \sqrt{\omega_0 \tau_{\text{VR}}'/8}$. This approximate result implies $\omega_0 \tau_{\text{VR}}' \gtrsim 8$ is needed for metastable behavior; however, the rigorous criterion is given in Eq. (12).

IV. NONLINEAR COMPUTATIONAL RESULTS WITH TRANSIENT PERTURBATION

A. Mode Penetration

In this section we investigate the effect of a transiently evolving magnetic perturbation. For these calculations, we initialize a configuration with $B_{\text{ext},0} = 3 \times 10^{-3} B_{\text{norm}}$, which produces, in steady state, a high-slip metastable equilibrium consistent with Eq. (11). We note here that for computations (not shown) with an initial time-asymptotic equilibrium outside of the metastable region, the system evolves in response to a transient perturbation, but always returns to the initial, stable equilibrium.

Defining a time shifted to the beginning of the transient $t' \equiv t - t_{\text{T}}$, where the transient begins at t_{T} , we prescribe the addition of a transient perturbation to the initial perturbation as

$$B_{\text{ext}}(t') = B_{\text{ext},0} T_{\text{NIM}}(t, \tau_0) + B_{\text{ext},\text{T}} T_{\text{NIM}}(t', \tau_{\text{T}}) \text{H}(t') - B_{\text{ext},\text{T}} T_{\text{NIM}}[t' - \Delta t_{\text{T}}, \tau_{\text{T}}] \text{H}[t' - \Delta t_{\text{T}}], \quad (15)$$

where $\text{H}(t)$ is the Heaviside step function and the transient has a characteristic rise and fall time τ_{T} , a magnitude $B_{\text{ext},\text{T}}$, and a duration Δt_{T} . The motivation for this form is to model a transient MHD event with a resonant magnetic component with characteristic temporal extent Δt_{T} . A similar parameterization is implemented for the tangential electric field for consistency with Faraday's law. The form of this perturbation is shown in Fig. 2a, with $\tau_{\text{T}} = 6.9 \tau_{\text{A}}$, $B_{\text{ext},\text{T}} = 9.0 B_{\text{ext},0}$, and $\Delta t_{\text{T}} = 6.9 \times 10^2 \tau_{\text{A}}$. These traces correspond to the value of $B_{\text{ext}} \equiv B_{x,1}(x = -a, y = L_y/2)$ recorded every time step.

For this transient magnetic perturbation, the resulting evolution for the magnitude of the y -dependent, $\sim \sin(k_y y)$ magnetic field $|B_{\text{res}}|$ and the net y -independent flow frequency ω_{res} at the resonant surface $x = 0$ are displayed by the solid (blue) traces in Fig. 2b-c, respectively. This computation is referred to as the ‘‘NIMROD standard case’’ throughout the rest of the paper. Values of these nonlocal parameters are calculated by recording $B_{x,1}$ and $V_{y,1}$ at three points every NIMROD computed time step: $N_1 = N(x = 0, y = L_y/2)$,

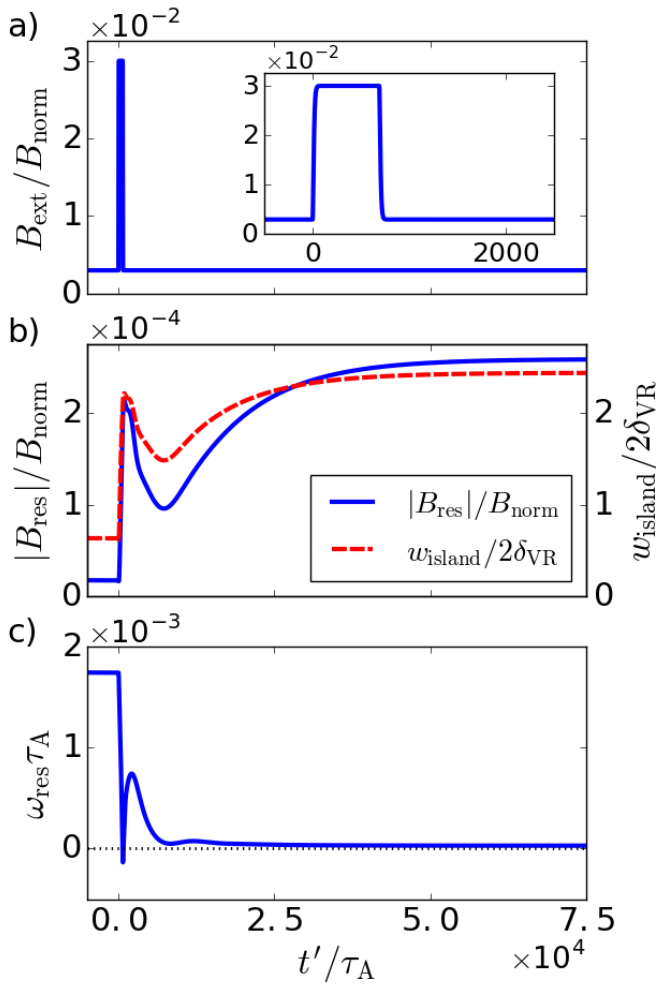


FIG. 2. Evolution of a) the externally applied magnetic field B_{ext} , b) the field response at the resonant surface $|B_{\text{res}}|$, and c) the flow frequency at the resonant surface ω_{res} . The dashed (red) trace in b) indicates the full width of the magnetic island. The transient perturbation causes the transition from a high-slip, flow-screened metastable state with a magnetic island thinner than the dissipation layer width to a low-slip, field-penetrated metastable state with a nonlinear island.

$N_2 = N(x=0, y=0)$, $N_3 = N(x=0, y=-L_y/2)$ for $N = B_{x,1}, V_{y,1}$. Then, we assume the magnetic field and flow have forms given by

$$B_{x,1}(x=0, y) \simeq |B_{\text{res}}| \sin(k_y y + \varphi_B), \quad (16a)$$

$$V_{y,1}(x=0, y) \simeq V_{\text{res}} + V_{\text{rec}} \sin(k_y y + \varphi_V), \quad (16b)$$

where V_{res} (V_{rec}) is the magnitude of the net (y -dependent) flow due to FMR of the magnetic field B_{ext} , and φ_B (φ_V) is the phase difference between $B_{x,1}$ (the y -dependent part of $V_{y,1}$) and B_{ext} . Profiles of the magnetic field and flow at $x=0$ (not shown) indicate Eqs. (16a-b) are generally good approximations. With the above assumptions, the magnitude of the resonant magnetic field and net flow frequency at the resonant surface are given in terms of local quantities by $|B_{\text{res}}| = \sqrt{B_1^2 + B_2^2}$ and $\omega_{\text{res}} = k_y[V_{y,0} + (V_1 + V_3)/2]$. The derived value of $|B_{\text{res}}|$ is used to calculate the full island width at the resonant surface shown by the dashed (red) trace in Fig. 2b, according to $w_{\text{island}} \equiv 4(L_{\text{sh}}|B_{\text{res}}|/k_y B_0)^{1/2}$,

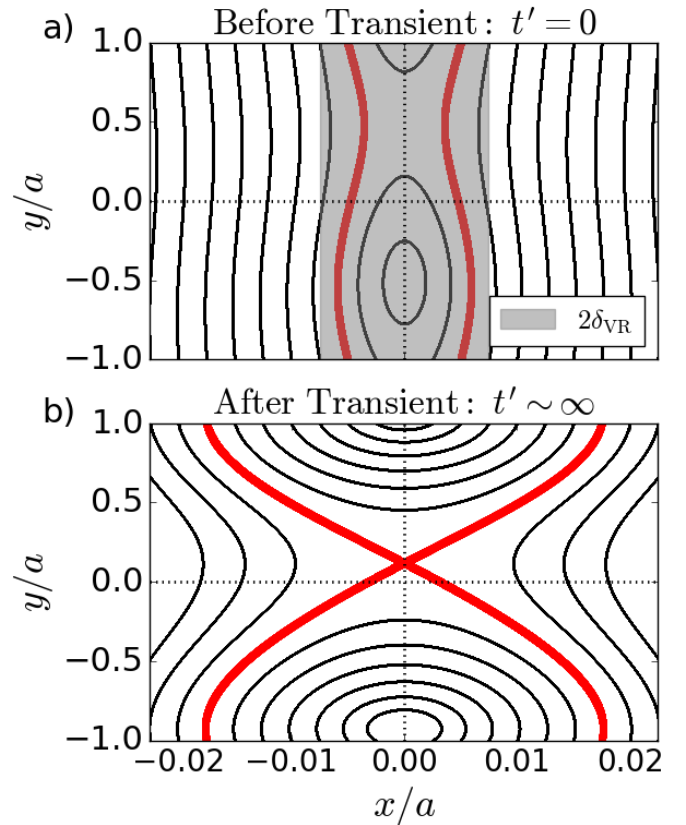


FIG. 3. Poincaré plots of the magnetic field structure in the computation shown in Fig. 2 for time-asymptotic metastable states a) just before the transient perturbation and b) long after the transient. The thick (red) contours indicate the approximate locations of the island separatrices. The externally applied field is the same in both plots, and the transient has caused the transition from the flow-screened, linear island in a) to the mode penetrated, nonlinear island in b).

where $L_{\text{sh}} \equiv 1/\{d/dx[B_y(x)/B_{0,z}]\}_{x=0} = 100 L_{\text{norm}}$ is the magnetic shear length.

Figure 2 shows that the effect of the applied external transient field is to precipitate the transition from a flow-screened state to a mode-penetrated state. On the time scale of the duration of the transient perturbation, the flow frequency drops through zero. After the transient, there is a partial rebound of the flow frequency, which settles to a small but nonzero value as the time-asymptotic state is approached. This evolution is reminiscent of a damped-driven oscillator. The magnetic field response at the resonant surface evolves over various time scales. Following the application of the external transient, the field response increases rapidly until it decreases slightly as the flow rebounds. Interestingly, the field response does not vary concomitantly with the flow frequency, indicating the nonlinear evolution is more complex than the linear flow-scaling of Eq. (7). As the flow returns to a small value at about $t' = 7 \times 10^3 \tau_A$, the field response evolves on a longer time scale consistent with nonlinear Rutherford evolution [50].

The transient perturbation causes the magnetic island at the rational surface, which is initially thinner than the dissipation layer, to grow into a nonlinear island. This is

directly observed in the Poincaré plots shown in Fig. 3. These trajectories are initialized at evenly spaced points in the computational domain and are not representative of the magnetic field density, only the topology. Figure 3a shows the magnetic island in the time-asymptotic state before the transient perturbation, and Fig. 3b shows the island in the time-asymptotic state following the transient. The approximate island separatrix is shown in each figure by the thick (red) trace. Before the transient the island is thinner than the dissipation layer, as indicated by the grey region, and wider than it following the transient. Additionally, the location of the X-point has evolved from its initial location. In the flow-screened case, the X-point of the island is near $\pi/2$ out of phase relative to the applied field, consistent with the predictions of Eq. (7). Following the FMR, the X-point of the island nearly corresponds to the phase of the applied field, consistent with the evolution of the flow profile.

During the transient perturbation, the flow frequency at the rational surface evolves rapidly. Because of viscosity, the local flow change dissipates, causing the flow profile to evolve, which in turn causes the viscous force to evolve according to Eq. (6b). Figure 4 shows flow profiles in x at the value of y where $\sin(k_y y + \varphi_V) = 0$ and the flow profile in y has a polarity consistent with flows at a reconnection X-point. We note that this location is offset from the null in the reconnected magnetic field $B_{x,1}$ due to the eddy currents present in the initial time-asymptotic equilibrium.

In Fig. 4 the dot-dashed (blue) and solid (green) traces indicate the time asymptotic flow profile before and after the transient perturbation, respectively, while the dotted (purple) and dashed (red) traces show the flow profile at $\Delta t_T/2$ and Δt_T during the transient perturbation. Figure 4a also shows that the no-slip boundary condition is moved inward to $|x| \simeq a_\nu$ due to the viscosity profile, and that the time-asymptotic profiles are nearly linear in the vicinity of the resonant surface. Interestingly, during the transient perturbation, the flow frequency profile in the vicinity of the resonant surface has additional shaping that leads to larger forces according to Eq. (6b). This is better seen in Fig. 4b, which zooms in near the resonant surface to show the flow frequency profiles at the linear layer δ_{VR} . Consistent with Eq. (6b), the increased magnitude in the jump of the derivative of the flow frequency results in a significantly increased viscous force during the transient perturbation.

B. Sensitivity of Mode Penetration Threshold

We next vary the parameters of the transient RMP in order to determine the qualitative sensitivity of mode penetration induced by the transient perturbation. Consistent with intuition developed from considering the time asymptotic force balance, we expect that a larger magnitude transient $B_{\text{ext},T}$ will more effectively trigger mode penetration. Figure 5 shows a comparison between two computations with different magnitudes of the transient RMP. The solid (blue) trace is the NIMROD standard case with $B_{\text{ext},T} = 9 B_{\text{ext},0}$ and the dashed (red)

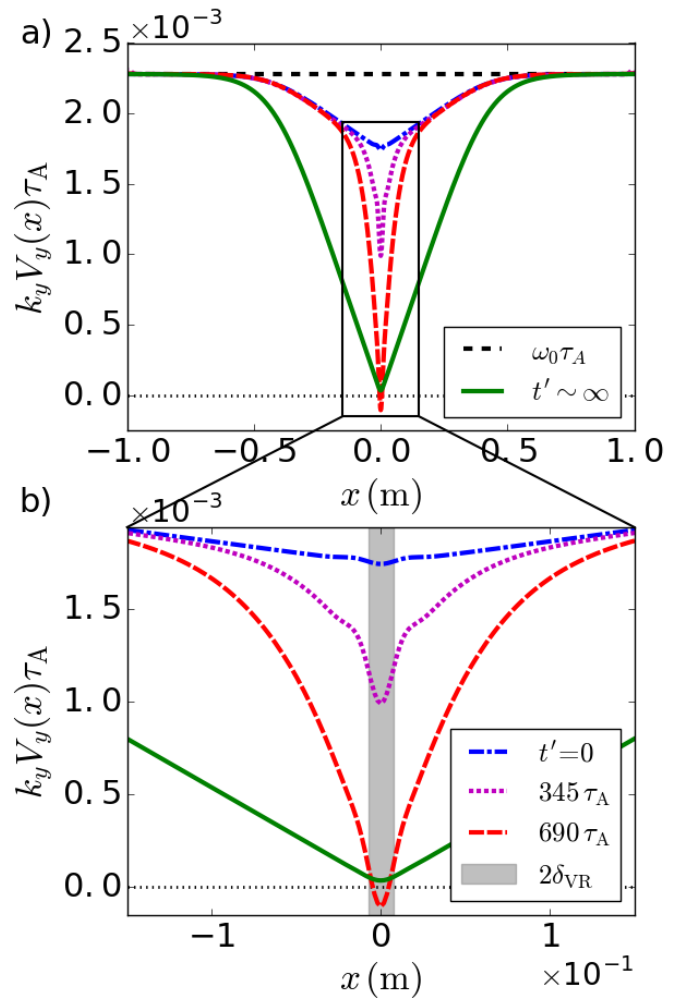


FIG. 4. Evolution of the flow profile during the externally applied transient magnetic field, where a) shows the entire range in x and b) zooms in near the dissipation layer. The short-dashed (black) trace corresponds to the initial flow frequency profile, the dotted-dashed (blue) trace corresponds to the initial time-asymptotic profile before the transient, the dotted (purple) and long-dashed (red) traces correspond to the evolving flow profiles during the transient, and the solid (green) trace corresponds to the time-asymptotic flow frequency profile long after the transient. The shaded (grey) region in b) indicates the width of the dissipation layer.

trace has $B_{\text{ext},T} = 7.75 B_{\text{ext},0}$, leaving all other parameters unchanged. As before, the computation with the larger magnitude transient penetrates. However, the computation with the lower magnitude transient exhibits similar field and flow responses during the duration of the transient, but post-transient evolves back to a flow-screened state. The lower magnitude transient case exhibits clear oscillations in the field response and flow frequency as it evolves towards its time asymptotic state, reinforcing the analogy to a damped-driven oscillator.

In Fig. 6, we zoom in to focus on the time duration during and just following the transient perturbation. In this figure we observe that the field and flow response during the transient are nearly identical, and it is only after the rebound following the transient that the flow in the computation with the smaller transient RMP evolves

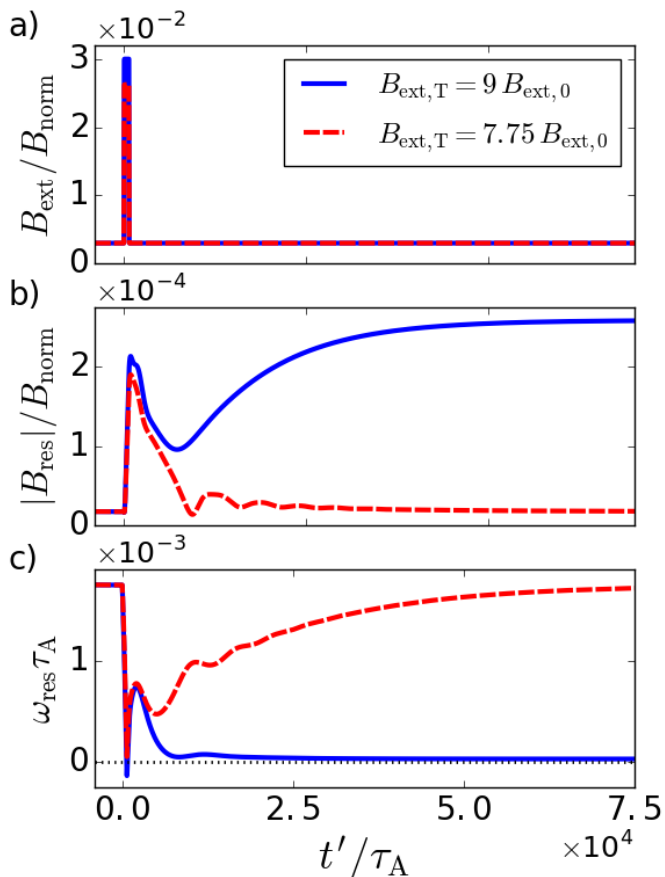


FIG. 5. Comparison between a) the externally applied magnetic field B_{ext} , b) the field response $|B_{\text{res}}|$, and c) the flow frequency at the rational surface ω_{res} for two computations with different magnitudes of the magnetic transient $B_{\text{ext},T}$, where the solid (blue) traces correspond to $B_{\text{ext},T} = 9 B_{\text{ext},0}$ and the dashed (red) traces correspond to $B_{\text{ext},T} = 7.75 B_{\text{ext},0}$. The effect of the larger transient is to precipitate a transition to a low-slip, field-penetrated state, while the smaller transient returns to the high-slip, flow-screened equilibrium.

back to a high-slip state. Additionally, in Fig. 6c it can be seen for the large transient that the flow frequency at the resonant surface crosses through zero, while it does not for the lower magnitude transient. However, as we discuss later, it is not necessary for this condition to be met for mode penetration to take place.

In our NIMROD computations, we have also parameterized the duration of the transient RMP Δt_T . Figure 7 shows a comparison between two computations with different durations of the transient RMP. The solid (blue) trace is the same as the NIMROD standard case with $\Delta t_T = 6.9 \times 10^2 \tau_A$ and the dashed (red) trace has $\Delta t_T = 4.8 \times 10^2 \tau_A$, leaving all other parameters unchanged. As before, the computation with the large duration transient exhibits mode penetration, while the smaller duration transient returns to the high-slip state. In this case, we observe that the flow frequency responds to a lesser degree because there is less time for it to evolve due to the shorter transient.

The last parameterization of the transient RMP that we test is the shape, by varying the rise and fall time

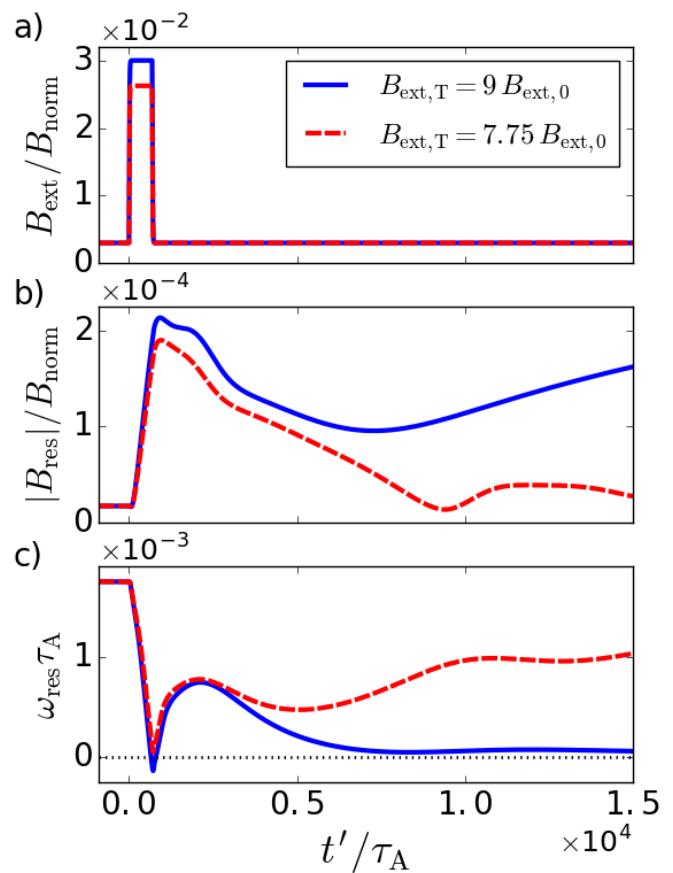


FIG. 6. Figure 5 zoomed in to focus on the time interval during and directly following the transient perturbation. Note the similar evolution of $|B_{\text{res}}|$ and ω_{res} during and just after the transient, before diverging into separate states.

τ_T . Figure 8 shows a comparison between two computations with different rise and fall times of the transient RMP. Both computations have $B_{\text{ext},T} = 7.75 B_{\text{norm}}$ and leave all other parameters unchanged. The solid (blue) trace has $\tau_T = 69.0 \tau_A$, and the dashed (red) trace is the same as the computation indicated by the dashed (red) trace in Figs. 5 and 6 with $\tau_T = 6.90 \tau_A$. Interestingly, while the computations have the same time integrated transient RMP and reach nearly the same field response during the transient as observed in Fig. 8b, the computation with the more “rounded” transient exhibits mode penetration, while the more “square” transient returns to a flow-screened state. The flow frequency response is significantly different between the two differently shaped transients; the more square transient initially decreases and then rebounds to a much larger extent than the rounded transient. Additionally, the rounded transient that induces mode penetration doesn’t have a flow response that goes through zero before rebounding. This is in contrast to previous results for mode penetration induced by a more squared transient. These results indicate that the detail of the evolution of the flow frequency is significant for mode penetration. Consistent with the sensitivity to transient magnitude, as the magnitude of the rounded transient is decreased to $B_{\text{ext},T} = 6.5 B_{\text{norm}}$ (not shown), there is a return to a flow-screened state.

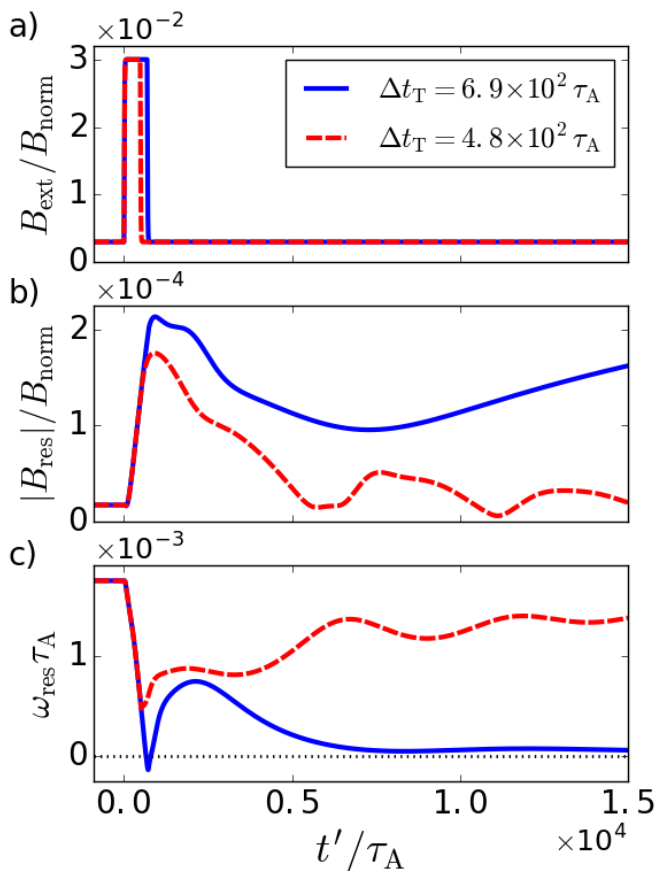


FIG. 7. Comparison between a) the externally applied magnetic field B_{ext} , b) the field response $|B_{\text{res}}|$, and c) the flow frequency at the rational surface ω_{res} for two computations with different durations of the magnetic transient $B_{\text{ext},T}$. Here, the solid (blue) traces correspond to $\Delta t_T = 6.9 \times 10^2 \tau_A$ and the dashed (red) traces correspond to $\Delta t_T = 4.8 \times 10^2 \tau_A$. The longer transient allows for more field response at the resonant surface and for the flow frequency to decrease further, compared to the shorter transient.

V. MODE PENETRATION DYNAMICS

In order to facilitate analytic interpretations of the temporally evolving NIMROD results presented in the preceding section, reduced models are developed here for the evolution of the key physical quantities in response to a transient $B_{\text{ext},T}$: $B_{\text{res}}(t)$ from a dynamic Faraday’s law, the flow $V_y(x, t)$ from the \hat{y} force balance, and the resultant ω_{res} at the $x = 0$ resonant surface. These results are used to estimate how large $B_{\text{ext},T}$ and its duration must be to induce a time-asymptotically, mode-penetrated, low-slip state. We first develop an approximate model of the initial [$t < 1/\omega_{\text{res}}(0)$] transient response in the vicinity of the resonant surface. Then we develop a more complete model that takes account of the temporal variation of ω_{res} and the global boundary conditions on the flow. Comparisons of the predictions of these two models to the preceding NIMROD results are presented throughout this section. We note that in this section, results are evaluated in terms of their SI units in addition to their dimensionless form, and stress that

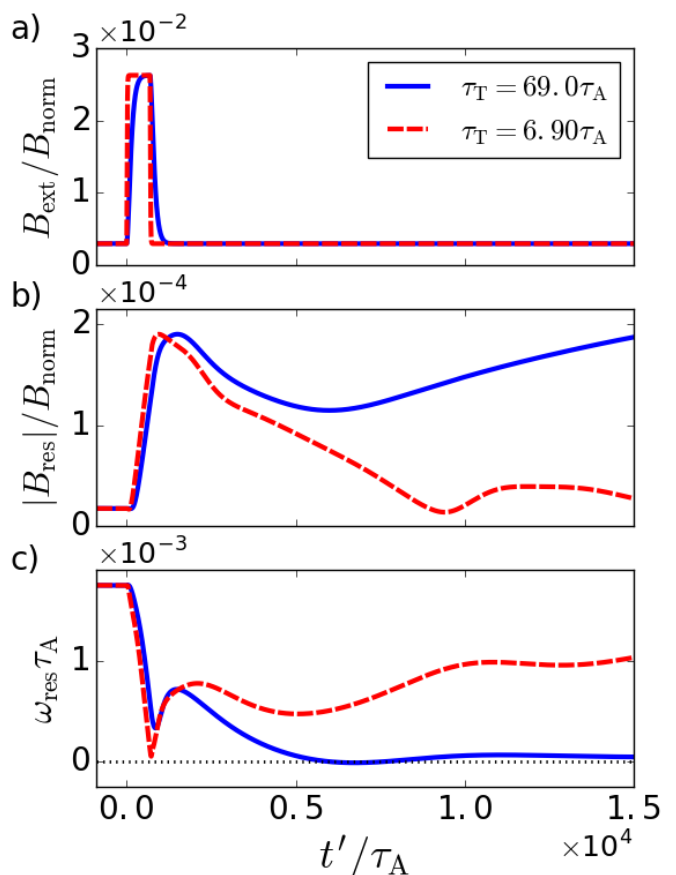


FIG. 8. Comparison between a) the externally applied magnetic field B_{ext} , b) the field response $|B_{\text{res}}|$, and c) the flow frequency at the rational surface ω_{res} for two computations with different turn on/off time scales for the magnetic transient $B_{\text{ext},T}$ given by Eq. (15). The solid (blue) traces correspond to $\tau_T = 69.0 \tau_A$ and the dashed (red) traces correspond to $\tau_T = 6.90 \tau_A$.

these values do not apply to any real experimental situation.

A. Equations Governing B_{res} and Flow Responses

The fundamental equations describing the dynamics of the resonant magnetic perturbation (RMP) and \hat{y} flow in response to a transient perturbation are obtained from components of Eqs. (1a-d). For times longer than $\tau_\eta \equiv S_{\text{sh}}^{1/3} \tau_{\text{sh}A} \simeq 7.0 \times 10 \tau_A \simeq 10^{-4}$ s, a “constant- ψ ” approximation is appropriate [13, 51] and the “matched asymptotic procedure” can be used to determine the response $B_{\text{res}}(t)$ at the resonant surface to a transient RMP. Because in the NIMROD standard case the response to $B_{\text{ext},T} = 9 B_{\text{ext},0}$ is turned on for $\Delta t_T = 6.9 \times 10^2 \tau_A \simeq 10^{-3}$ s, most of the responses occur in the constant- ψ regime and the asymptotic matching procedure [47] can be used.

A dynamic equation for the resonant field B_{res} is obtained from the induction equation using a combination of Eqs. (1b) and (1c) in the dissipation layer at the resonant surface. Performing an asymptotic matching of the

induction equation about the resonant surface [52] in a visco-resistive dissipation regime yields

$$\left[\frac{d}{dt'} + i\omega_{\text{res}}(t') + \frac{1}{\tau'_{\text{VR}}} \right] B_{\text{res}}(t') = \frac{a\Delta'_{\text{ext}}}{\tau_{\text{VR}}} B_{\text{ext}}(t'), \quad (17)$$

where we have employed a linear, asymptotic matching procedure accounting for the intrinsic tearing response ($\sim \Delta'_0$) and a contribution due to the applied field ($\sim \Delta'_{\text{ext}}$). Note that Eq. (17) assumes B_x is constant within the $\Delta x \cong \delta_{\text{VR}}$ dissipation layer at $x = 0$. We repeat for clarity that $t' = t - t_{\text{T}}$ indicates the time shifted to the beginning of the transient perturbation. We choose a general form for the evolution of the external field during the transient RMP $B_{\text{ext}}(t') = B_{\text{ext},0} + B_{\text{ext},\text{T}}T(t')$, where $B_{\text{ext},0}$ is the magnitude of the constant, initial RMP, $B_{\text{ext},\text{T}}$ is the magnitude of the transient RMP, and $T(t')$ is the time-dependence of the transient similar to that defined in Eq. (3c).

Magnetic reconnection induced by $B_{\text{ext},\text{T}}$ dominantly occurs in the very thin visco-resistive singular layer of width δ_{VR} on either side of the resonant surface initially. The flow profile $V_y(x, t')$ is determined from the \hat{y} -component of the momentum equation in Eq. (1a) which can be written as

$$\left[\frac{\partial}{\partial t'} - \frac{\partial}{\partial x} \left(\nu_0 \bar{\nu}(x) \frac{\partial}{\partial x} \right) \right] V_y(x, t') = \frac{\bar{F}_{y,\text{EM}}(x, t')}{\rho}. \quad (18)$$

Here, the LHS describes the viscous diffusion effects in response to the singular $J_z B_x$ EM force inside the dissipation layer on the RHS. The average EM force density over x and y is given by

$$\bar{F}_{y,\text{EM}}(x, t') = -\mathcal{I}m\{B_{\text{res}}^*(t')\} \frac{a\Delta'_{\text{ext}} B_{\text{ext}}(t')}{2(k_y a) \mu_0} \delta\{x\}. \quad (19)$$

The delta function $\delta\{x\}$ in Eq. (19) represents the infinitesimal singular layer width, making $\bar{F}_{y,\text{EM}}$ the local EM force density near the resonant surface. The average EM force density is calculated in an analogous way to Eq. (5) and related to the EM force per unit length by $\bar{F}_{y,\text{EM}} = \hat{F}_{y,\text{EM}} \delta\{x\} / L_y$.

Equation (18) is a diffusion equation for $V_y(x, t')$. It can be solved using a Green function $G(x, t'|x_0, t_0)$ which satisfies $(\partial/\partial t' - \partial^2/\partial x^2)G = \delta\{x - x_0\} \delta\{t' - t_0\}$. The formal solution of Eq. (18) is then given by

$$V_y(x, t') = \int_0^{t'} dt_0 \int_{-\infty}^{\infty} dx_0 G(x, t'|x_0, t_0) \frac{\bar{F}_{y,\text{EM}}(x_0, t_0)}{\rho}. \quad (20)$$

Possible boundary terms have been omitted presently because: 1) their effects are negligible near the resonant surface for short times, and 2) their effects are incorporated in Appendix B for use in the derivation of the general viscous force in Section VD.

B. Approximate Initial Dynamics Analysis

For the simplest possible model of the dynamic response to an externally applied transient $B_{\text{ext},\text{T}}$, five approximations will be made. First, we assume the flow

frequency at the resonant surface remains at its initial value during the transient, i.e., $\omega_{\text{res}}(t') \rightarrow \omega_{\text{res}}(0)$ in Eq. (17). Second, we assume $|\omega_{\text{res}}(0)\tau_{\text{VR}}| \gg | -a\Delta'_0 |$ so from Eq. (7) the initial resonant field response to the background $B_{\text{ext},0}$ is $B_{\text{res}}(0) \simeq (a\Delta'_{\text{ext}}) B_{\text{ext},0} / [i\omega_{\text{res}}(0)\tau_{\text{VR}}]$ and that the $1/\tau'_{\text{VR}}$ term in Eq. (17) can be neglected. Third, we assume the transient perturbation is a square pulse, i.e., that $T(t') = H\{t'\} - H\{t' - \Delta_T\}$. Then, the resulting approximate form of Eq. (17) can be solved using an $e^{i\varphi}$ integrating factor, in which $\varphi \equiv \omega_{\text{res}}(0)t'$. For $0 \leq t' < \Delta_T$ the result can be written as

$$B_{\text{res}}(t') \simeq \frac{a\Delta'_{\text{ext}} e^{-i\varphi}}{i\omega_{\text{res}}(0)\tau_{\text{VR}}} [B_{\text{ext},0} + B_{\text{ext},\text{tot}}(e^{i\varphi} - 1)]. \quad (21)$$

Here, the total applied external magnetic perturbation is $B_{\text{ext},\text{tot}} \equiv B_{\text{ext},0} + B_{\text{ext},\text{T}}$.

Fourth, in order to concentrate on the initial response it will be assumed that $\varphi \leq 1$. Then, the approximate imaginary part of $B_{\text{res}}(t')$ that is needed for determining the EM force is

$$\mathcal{I}m\{B_{\text{res}}^{\varphi \leq 1}(t')\} \simeq \frac{(a\Delta'_{\text{ext}}) B_{\text{ext},\text{T}}}{\omega_{\text{res}}(0)\tau_{\text{VR}}} \times \left\{ \frac{[\omega_{\text{res}}(0)t']^2}{2} + \frac{B_{\text{ext},0}}{B_{\text{ext},\text{T}}} \right\}. \quad (22)$$

Here, the $[\omega_{\text{res}}(0)t']^2$ term represents the out-of-phase response directly driven by the transient perturbation and the last term is caused by the initial perturbation $B_{\text{res},0}$. Using this last result in Eq. (19), the approximate averaged EM force can be written as

$$\frac{\bar{F}_{y,\text{EM}}^{\varphi \leq 1}}{\rho} \simeq - \frac{V_{\text{res}}(0)^2 T_{\mathcal{E}}}{4(k_y a) [\omega_{\text{res}}(0)\tau_{\text{VR}}]} \times \left\{ [\omega_{\text{res}}(0)t']^2 + \frac{2B_{\text{ext},0}}{B_{\text{ext},\text{T}}} \right\} \delta\{x\} \mathcal{H}\{t'\}. \quad (23)$$

Here, the ratio of the effective transient magnetic perturbation energy to initial flow energy is $T_{\mathcal{E}} \equiv [(a\Delta'_{\text{ext}})^2 B_{\text{ext},\text{tot}} B_{\text{ext},\text{T}} / 2\mu_0] / [\rho V_{\text{res}}(0)^2 / 2] \simeq 765$. Here, $T_{\mathcal{E}}$ is evaluated for the NIMROD standard case where $B_{\text{ext},\text{T}} = 9 B_{\text{ext},0}$ and from Fig. 2c $\omega_{\text{res}}(0)\tau_{\text{A}} \simeq 1.75 \times 10^{-3}$, which yields $\omega_{\text{res}}(0) \simeq 1200$ rad/s and $V_{\text{res}}(0) \equiv \omega_{\text{res}}(0)/k_y = a\omega_{\text{res}}(0)/\pi \simeq 384$ m/s.

Fifth, for $|x| \ll a$ the local Green function $G(x, t'|x_0, t_0) = e^{-(x-x_0)^2/4\nu_0(t'-t_0)} / \sqrt{4\pi\nu_0(t'-t_0)}$ can be used in solving Eq. (18). Using this infinite medium Green function and Eq. (23) in Eq. (20) yields (see Appendix A for details) for the approximate, local flow response $\Delta V_y \equiv V_y(x, t') - V_{\text{res}}(0)$ to the transient magnetic perturbation $B_{\text{ext},\text{T}}$:

$$\frac{\Delta V_y(x, t)}{V_{\text{res}}(0)} = - \frac{(\tau_{\mu}/\tau_{\text{VR}}) T_{\mathcal{E}}}{8\sqrt{\pi} (k_y a)^2 [\omega_{\text{res}}(0)\tau_{\mu}]^{1/2}} f_V(x, t'), \quad (24)$$

$$f_V(x, t') \equiv [\omega_{\text{res}}(0)t']^{1/2} \times \left\{ \frac{16}{15} [\omega_{\text{res}}(0)t']^2 F_{\text{VT}} + \frac{4B_{\text{ext},0}}{B_{\text{ext},\text{T}}} F_{\text{V0}} \right\}. \quad (25)$$

Here, $F_{\text{VT}}(x, t')$ and $F_{\text{V0}}(x, t')$ are spatially evolving factors calculated in Appendix A. They are both unity at

$x = 0$. As discussed in Appendix A, the spatial profiles these factors produce correspond approximately to the NIMROD flow responses shown in Fig. 4b.

Finally, we hypothesize that for the transient RMP $B_{\text{ext},T}$ to induce a time-asymptotic low-slip (mode penetrated) state, the EM force it produces must reduce flow at the resonant surface to near zero, i.e., yield $\Delta V_y(0, t')/V_{\text{res}}(0) \simeq -1$. Assuming $B_{\text{ext},0}$ lies in the metastable region, using the result in Eq. (24) at $x = 0$, this criterion can be written as

$$f_V(0, t') \frac{B_{\text{ext,tot}} B_{\text{ext},T}}{B_{0,z}^2} \gtrsim C_B, \text{ in which} \quad (26)$$

$$C_B \equiv \frac{8\sqrt{\pi} (k_y a)^2 [\omega_{\text{res}}(0) \tau_\mu]^{1/2} V_{\text{res}}(0)^2}{(\tau_\mu / \tau_{\text{VR}}) (a \Delta'_{\text{ext}})^2 c_A^2} \simeq 7.95 \times 10^{-8}. \quad (27)$$

Here, $t' \simeq \min\{\Delta t_T, 1/\omega_{\text{res}}(0), \tau'_{\text{VR}}\}$ is the minimum of the: 1) time $\Delta t_T = 6.9 \times 10^2 \tau_A = 10^{-3}$ s that $B_{\text{ext},T}$ is applied, 2) inverse of the initial flow frequency $1/\omega_{\text{res}}(0) = 5.75 \times 10^2 \tau_A = 8.3 \times 10^{-4}$ s, after which the response becomes oscillatory, and 3) relevant visco-resistive tearing time $\tau'_{\text{VR}} = 8.56 \times 10^3 \tau_A = 1.24 \times 10^{-2}$ s, after which the response transitions into a slower nonlinear [Rutherford [50]] growth regime.

For $t' = 1/\omega_{\text{res}}(0)$ the requirement in Eq. (26) is $B_{\text{ext},T} \gtrsim 2.05 \times 10^{-2} B_{\text{norm}} \simeq 6.8 B_{\text{ext},0}$, in which about two thirds is caused by direct transient effects and a third is due to the initial perturbation. This result is in rough agreement with the time-asymptotic results for various ratios of $B_{\text{ext},T}/B_{\text{ext},0}$ shown in the preceding section. These comparisons indicate that while the criterion in Eq. (26) can provide a rough guide for the conditions needed for transition into a time-asymptotic low-slip state, the nonlinear dynamics of the magnetic field and flow responses, particularly during and just after the transient is being turned off, is important for precise determinations of them.

C. General Time-Dependent EM Force

The preceding analysis made five approximations to explore the initial temporal dynamics of the response to an externally applied resonant magnetic perturbation. This subsection and the following ones remove these five approximations in order to develop a more complete analytic-based model of the transient responses within a linear, constant- ψ formulation.

The evolution of the EM force due to a transient perturbation is fundamentally governed by Eq. (6a) or (19). To evaluate the evolution of the EM force, we must first evaluate the evolution of the magnetic field according to the induction equation, Eq. (17). With the general form for the external field Eq. (15), Eq. (17) can be solved

directly by use of an integrating factor to yield

$$B_{\text{res}}(t') = \frac{\Delta'_{\text{ext}}}{-\Delta'_0} \exp\left[-\frac{t'}{\tau'_{\text{VR}}} - i\varphi_{\text{res}}(t')\right] \left\{ \frac{B_{\text{ext},0}}{1 + i\omega_{\text{res}}(0)\tau'_{\text{VR}}} + \frac{B_{\text{ext},0}}{\tau'_{\text{VR}}} \int_0^{t'} ds \exp\left[\frac{s}{\tau'_{\text{VR}}} + i\varphi_{\text{res}}(s)\right] + \frac{B_{\text{ext},T}}{\tau'_{\text{VR}}} \int_0^{t'} ds \exp\left[\frac{s}{\tau'_{\text{VR}}} + i\varphi_{\text{res}}(s)\right] T(s) \right\}, \quad (28)$$

where the initial condition on B_{res} at $t' = 0$ is given by Eq. (7), the flow phase $\varphi_{\text{res}}(t')$ is defined according to

$$\varphi_{\text{res}}(t') \equiv \int_0^{t'} ds \omega_{\text{res}}(s), \quad (29)$$

the time-dependent form of the φ appearing in Eq. (21), and we choose $\varphi_{\text{res}}(0) = 0$. The first term in Eq. (28) is the field response due to the initial external field $B_{\text{ext},0}$ modified by the evolving flow phase, the second term is the field response due to the initial RMP affected by the dynamics precipitated by the transient RMP $B_{\text{ext},T}$, and the third term is the field response due to the transient perturbation. Equation (28) can be used to calculate the EM force according to Eq. (6a), which yields

$$\begin{aligned} \hat{F}_{y,\text{EM}}(t') = & -\frac{L_y}{2\mu_0 k_y} \frac{(\Delta'_{\text{ext}})^2}{-\Delta'_0} [B_{\text{ext},0} + B_{\text{ext},T} T(t')] \\ & \times \exp\left(-\frac{t'}{\tau'_{\text{VR}}}\right) \left\{ \frac{B_{\text{ext},0}}{1 + [\omega_{\text{res}}(0)\tau'_{\text{VR}}]^2} \left[\sin \varphi_{\text{res}}(t') \right. \right. \\ & + \left. \left. \omega_{\text{res}}(0)\tau'_{\text{VR}} \cos \varphi_{\text{res}}(t') \right] \right. \\ & + \frac{B_{\text{ext},0}}{\tau'_{\text{VR}}} [\sin \varphi_{\text{res}}(t') \Phi_{C,0}(t') - \cos \varphi_{\text{res}}(t') \Phi_{S,0}(t')] \\ & \left. + \frac{B_{\text{ext},T}}{\tau'_{\text{VR}}} [\sin \varphi_{\text{res}}(t') \Phi_{C,T}(t') - \cos \varphi_{\text{res}}(t') \Phi_{S,T}(t')] \right\}, \quad (30) \end{aligned}$$

where auxiliary variables are defined as

$$\frac{d}{dt'} \Phi_{C,0}(t') = \exp\left(\frac{t'}{\tau'_{\text{VR}}}\right) \cos \varphi_{\text{res}}(t'), \quad (31a)$$

$$\frac{d}{dt'} \Phi_{S,0}(t') = \exp\left(\frac{t'}{\tau'_{\text{VR}}}\right) \sin \varphi_{\text{res}}(t'), \quad (31b)$$

$$\frac{d}{dt'} \Phi_{C,T}(t') = \exp\left(\frac{t'}{\tau'_{\text{VR}}}\right) \cos \varphi_{\text{res}}(t') T(t'), \quad (31c)$$

$$\frac{d}{dt'} \Phi_{S,T}(t') = \exp\left(\frac{t'}{\tau'_{\text{VR}}}\right) \sin \varphi_{\text{res}}(t') T(t'), \quad (31d)$$

subject to initial conditions $\Phi_{C,0}(0) = \Phi_{S,0}(0) = \Phi_{C,T}(0) = \Phi_{S,T}(0) = 0$.

Complementary to the discussion on the form of Eq. (28), the form of Eq. (30) implies that the EM force during the transient perturbation is composed of three parts. The first component is due to the penetration of the initial external field $B_{\text{ext},0}$, whose phase shifts due to the evolving flow frequency to affect the EM force. The

second component is due to the penetration of the initial external field during the dynamics precipitated by the transient external field $B_{\text{ext},T}$, whose magnitude is screened and phase-shifted due to the evolving flow frequency to affect the EM force. Lastly, the third component is due to the penetration of the transient external field whose magnitude is screened and phase-shifted due to the evolving flow frequency to affect the EM force.

D. General Time-Dependent Viscous Force

A Green function approach could in principle be used as in Subsection V B. However, it would involve an evolving $\omega_{\text{res}}(s)$ and hence $\varphi(t')$ inside the time integral in (20) and thus yield a complicated integro-differential equation for $V_y(x, t)$. Thus, we instead use a more direct procedure for determining the viscous force effects.

In order to evaluate the evolution of the viscous force defined in Eq. (6b), we must determine the evolving flow profile. In Appendix B we employ an infinite-series eigenfunction expansion to solve for the time-dependent flow profile in terms of $V_{\text{res}}(t)$ at the rational surface, resulting in Eq. (B16); $V_{\text{res}}(t)$ is solved for self-consistently in the next subsection, including the effect of the EM force. Because we begin in a time-asymptotic metastable state at $t' = 0$, the initial flow profile is linear in x for $0 < |x| < a_\nu$ and the first term in the infinite sum of Eq. (B16) vanishes. Next, we observe that the flow profile is even about $x = 0$, so taking the derivative results in an odd profile, reducing the jump condition in Eq. (6b) to $2\partial V_y/\partial x|_{x=0}$. Thus, Eq. (6b) yields

$$\hat{F}_{y,V}(t') = \frac{2L_y\rho\nu_0}{k_y a_\nu} \left[\omega_0 - \omega_{\text{res}}(t') - 2 \sum_{n=1}^{\infty} \int_0^{t'} ds \frac{d\omega_{\text{res}}(s)}{ds} e^{-(n\pi)^2 \frac{t'-s}{\tau_\nu}} \right]. \quad (32)$$

For sufficiently long times $d\omega_{\text{res}}(s)/ds$ can be taken out of the integrand. Because the exponential is the only factor dependent on the index n , the sum can be taken inside the integral and exclude $d\omega_{\text{res}}(s)/ds$. As s approaches t' , this infinite sum approaches ∞ . Thus, the integral of Eq. (32) weights $d\omega_{\text{res}}(s)/ds$ more strongly as s approaches t' , and $d\omega_{\text{res}}(t')/dt'$ can be pulled outside of the integral. With this assumption, simplifying yields

$$\hat{F}_{y,V}(t') = \frac{2L_y\rho\nu_0}{a_\nu k_y} \left\{ \omega_0 - \omega_{\text{res}}(t') + 2\tau_\nu \frac{d\omega_{\text{res}}(t')}{dt'} + \sum_{n=1}^{\infty} \frac{1}{(n\pi)^2} \left[e^{-(n\pi)^2 \frac{t'}{\tau_\nu}} - 1 \right] \right\}, \quad (33)$$

where $\tau_\nu \equiv a_\nu^2/\nu_0$ is the global viscous time with a nonuniform viscosity profile, and the infinite sum is convergent. The first term in Eq. (33) has the form of the time-asymptotic viscous force specified in Eq. (10) for evolving $\omega_{\text{res}}(t')$, while the second term is an additional contribution to the viscous force due to the transiently-evolving flow profile. The time-dependence of this second

term indicates that it is only important for times short compared to $\tau_\nu/(k_y a)^2 = 3.25 \times 10^3 \tau_A = 4.7 \times 10^{-3}$ s.

E. Self-Consistent Force Balance Evolution

The integral of Eq. (1a) over the reconnecting layer can now be solved for the evolution of the flow at the resonant surface due to a transient magnetic perturbation. This will determine whether the mode penetrates and locks or if there is a subsequent return to a flow-screened state. We begin by applying Eq. (5) to Eq. (1a), which balances inertia with the EM and viscous forces per unit length according to

$$\frac{\delta_{\text{VR}} L_y \rho}{k_y} \frac{d\omega_{\text{res}}(t')}{dt'} = \hat{F}_{y,\text{EM}}(t') + \hat{F}_{y,V}(t'). \quad (34)$$

The EM force in Eq. (30) is evaluated with the form of the RMP field given in Eq. (15) for eventual comparisons with NIMROD computations, and the viscous force is given by Eq. (33). Together with Eq. (29) for the evolution of the flow phase, Eqs. (31a-d) for the evolution of the auxiliary variables, and the initial conditions $\omega_{\text{res}}(0)$ from the high-slip, metastable equilibrium from Eq. (11), $\varphi_{\text{res}}(0) = 0$, and $\Phi_{C/S,0/T}(0) = 0$, Eq. (34) can be solved as part of a system of coupled nonlinear ordinary differential equations (ODEs). To solve this system, we use the `odeint` routine from the `scipy.integrate` subpackage developed in the Python programming language. `Odeint` solves systems of ODEs using the LSODA solver from the FORTRAN library `odepack` [53]. The infinite sum in Eq. (33) is truncated when the next term in the sum is less than 0.02% of the total, which is found to be a good estimate.

The solution of the system of equations detailed above is shown in Fig. 9 for the NIMROD standard case with $B_{\text{ext},T} = 9 B_{\text{ext},0}$ and $\Delta t_T = 6.90 \times 10^2 \tau_A$. In Fig. 9a, the solid (blue) trace shows the evolution of the flow frequency and the dashed (red) trace shows the evolution of the flow frequency phase. The transient perturbation extends from $t' = 0$ to the vertical dashed line at $t' = \Delta t_T$. During the transient the flow frequency decreases through zero, and after the transient the flow frequency recoils before decreasing to near zero, consistent with a mode locked state.

Figure 9b shows the evolution of the calculated forces in the model, where the dashed (blue) trace is F_{EM} and corresponds to Eq. (30), the dashed-dotted (green) trace is F_V and corresponds to Eq. (33), and the solid (black trace) is $F_{\text{Total}} \times 10$ and corresponds to the net force on the RHS of Eq. (34). F_{Total} is self-consistent with the evolution of the analytic flow frequency. At the beginning of the transient, the magnitude of F_{EM} increases rapidly, followed by F_V to limit the change in the flow frequency. Just after the transient, the magnitude of F_{EM} decreases rapidly while the viscous force remains large, leading to the recoil in the flow frequency. Because the flow frequency phase increases when the flow frequency increases above zero, the magnitude of the EM force also rebounds, which forces the flow frequency back towards zero. Lastly, F_V asymptotes to the time-asymptotic

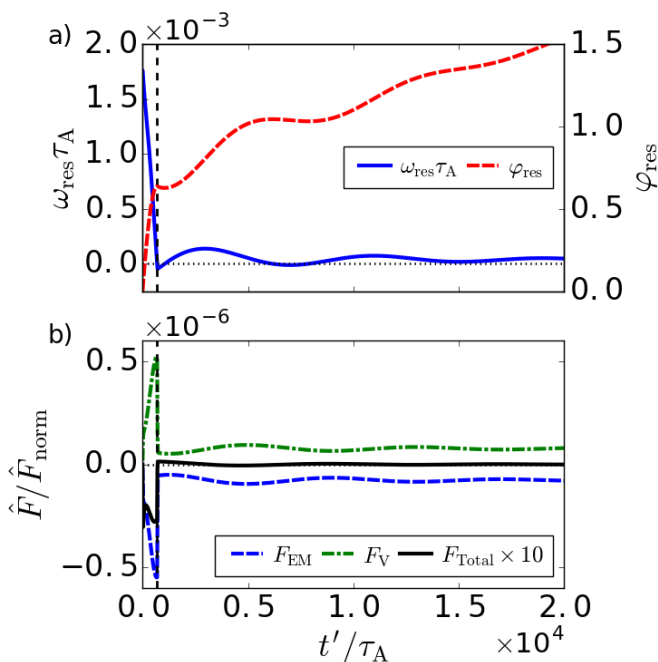


FIG. 9. Analytical predictions for the evolution due to an externally-applied magnetic transient with magnitude $B_{\text{ext},T} = 9 B_{\text{ext},0}$, which undergoes mode penetration. a) The flow frequency and the flow frequency phase corresponding to the solid (blue) and dashed (red) traces, respectively, according to Eqs. (34) and (29). b) The dashed (blue) trace is F_{EM} and corresponds to Eq. (30), the dashed-dotted (green) trace is $F_{V,T}$ and corresponds to Eq. (33), and the solid (black trace) is $F_{\text{Total}} \times 10$ and corresponds to the scaled net force.

value consistent with the form of the time-dependence in Eq. (33), and the locked system has F_{EM} balancing F_V in the time-asymptotic, low-slip, metastable equilibrium.

Decreasing the magnitude of the transient to $B_{\text{ext},T} = 4.5 B_{\text{ext},0}$ yields the model solution plotted in Fig. 10, which exhibits a return to a high-slip, flow-screened equilibrium. For values of $B_{\text{ext},T}$ larger than $4.5 B_{\text{ext},0}$, mode penetration occurs. Thus, compared to the threshold for mode penetration seen in NIMROD computations at approximately $B_{\text{ext},T} = 7.75 B_{\text{ext},0}$ in Fig. 5, this model prediction differs by less than a factor of 2. While the evolution of ω_{res} toward the time-asymptotic state of the cases shown in Figs. 9 and 10 are distinct, because the evolution of the forces are subtle, defining a precise threshold for mode penetration is challenging. Furthermore, splitting the EM force into separate components due to $B_{\text{ext},0}$ and $B_{\text{ext},T}$ consistent with Eq. (30) (not shown) also indicates a subtle evolution of the forces, consistent with an indistinct threshold for mode penetration.

F. Comparisons With Numerical Results

In this subsection, we directly compare results from the NIMROD standard case presented in Section IV to analytical predictions developed in the preceding subsections. For the duration of the transient, both models derived in previous subsections are applicable. Figure

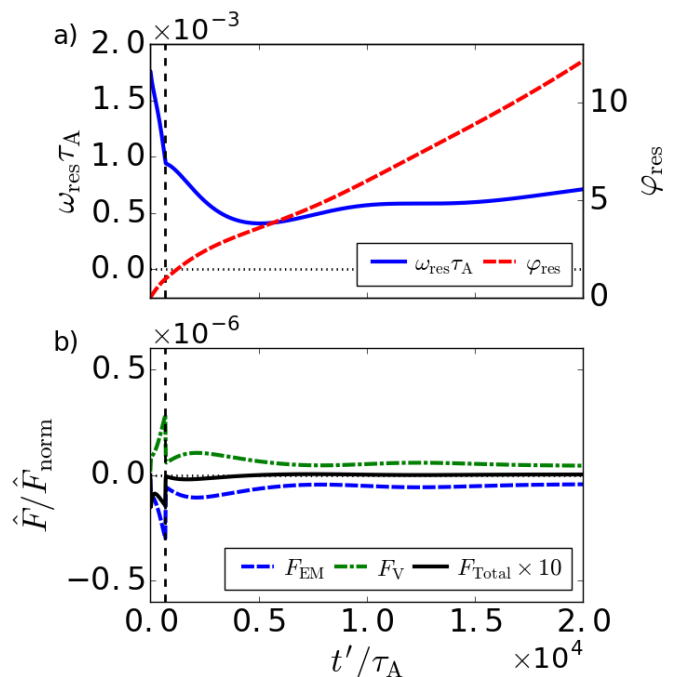


FIG. 10. Analytical predictions for the evolution due to an externally-applied magnetic transient with magnitude $B_{\text{ext},T} = 4.5 B_{\text{ext},0}$, which returns to a high-slip, flow-screened equilibrium. a) The flow frequency and the flow frequency phase corresponding to the solid (blue) and dashed (red) traces, respectively, according to Eqs. (34) and (29). b) The dashed (blue) trace is F_{EM} and corresponds to Eq. (30), the dashed-dotted (green) trace is F_V and corresponds to Eq. (33), and the solid (black trace) is $F_{\text{Total}} \times 10$ and corresponds to the scaled net force.

11 shows solid (blue) traces corresponding to NIMROD computations, dash-dotted (green) traces corresponding to the model assuming ω_{res} is constant in F_{EM} , and dashed (red) traces for the model with self-consistently evolving ω_{res} . The time interval from $t' = 0$ to the vertical dashed line at $t' = \Delta t_T$ indicates the duration of the transient.

We find good agreement between the models for the field response, as observed in Fig. 11a, where the dash-dotted trace is Eq. (21) and the dashed trace is Eq. (28). The deviation at the beginning of the transient is due to the existence of a nonconstant- ψ regime for $t' < \tau_\eta$, which is neglected in the analytical modeling as discussed previously. However, we find some discrepancy in the flow frequency evolution shown in Fig. 11b. The dash-dotted trace corresponding to Eq. (24), which omits the $T_{\text{NIM}}(t)$ of the transient, is qualitatively similar but significantly different from the NIMROD result, while the dashed trace corresponding to the self-consistent solution to Eq. (34) is more consistent with the NIMROD results.

Looking over a longer time scale, Fig. 12 shows the computational results of the NIMROD standard case by solid (blue) traces and the self-consistent model predictions by dashed (red) traces. After the transient, Fig. 12a indicates a qualitative difference in the evolution of the field response. Whereas NIMROD results show a dip in $|B_{\text{res}}|$ following the transient, the analytic results show a

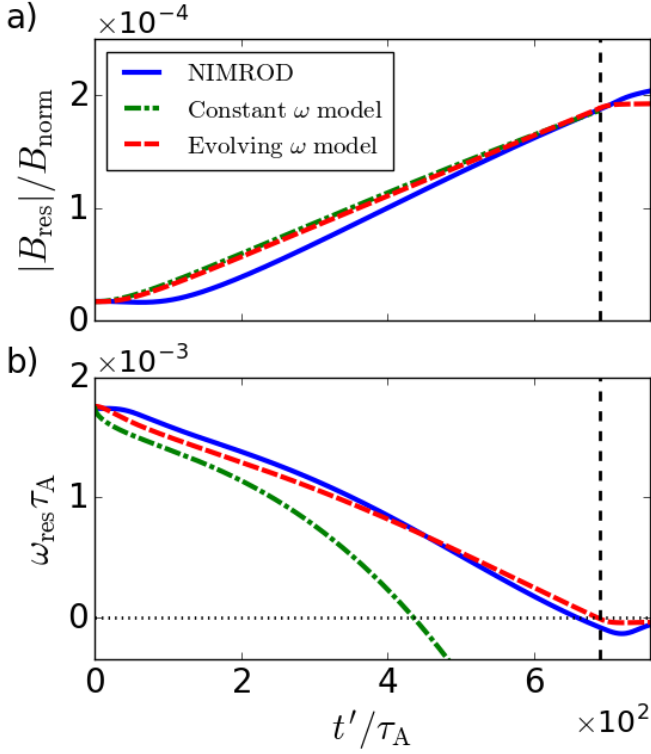


FIG. 11. Comparison between NIMROD results in the solid (blue) traces and model predictions using the constant- ω_{res} F_{EM} dash-dotted (green) traces and self-consistent evolving ω_{res} dashed (red) traces for a) the field response $|B_{\text{res}}|$ and b) the flow frequency at the resonant surface ω_{res} . While the results are qualitatively similar for the field response, the model employing an EM force assuming constant ω_{res} does not exhibit accurate ω_{res} evolution.

slow monotonic increase in the field response. The dip in the computational results correlates with the evolution of the flow frequency phase in Fig. 12c, which explicitly depends on the flow frequency in Fig. 12b. While the model prediction for ω_{res} rebounds and locks over a similar time scale, the computational result rebounds to a magnitude a factor of ~ 4 larger. This is directly captured in evolution of φ_{res} , which evolves slowly for the model prediction, while the computational result rapidly increases to a larger value following the transient. We posit that this discrepancy is due to a nonlinear phase slip of the island relative to the lab frame, as discussed in the next section.

G. Nonlinear Evolution of Magnetic Island

When \hat{F}_{EM} is large enough to force the flow toward the rest frame of B_{ext} (e.g., at about $t' \simeq 7.0 \times 10^3 \tau_A = 10^{-2}$ s in Fig. 2) and the magnetic island width $w \equiv 4[L_{\text{sh}}B_{\text{res}}/k_y B_{0,z}]^{1/2}$ is much larger than twice the dissipative layer width $2\delta_{\text{VR}}$ (e.g., for $t' \gg 2.0 \times 10^2 \tau_A = 3 \times 10^{-4}$ s in Fig. 2), one is in the nonlinear modified Rutherford regime. The modified Rutherford equation (MRE) that governs growth (or damping) of the island width in the slab model for a non-flowing plasma is

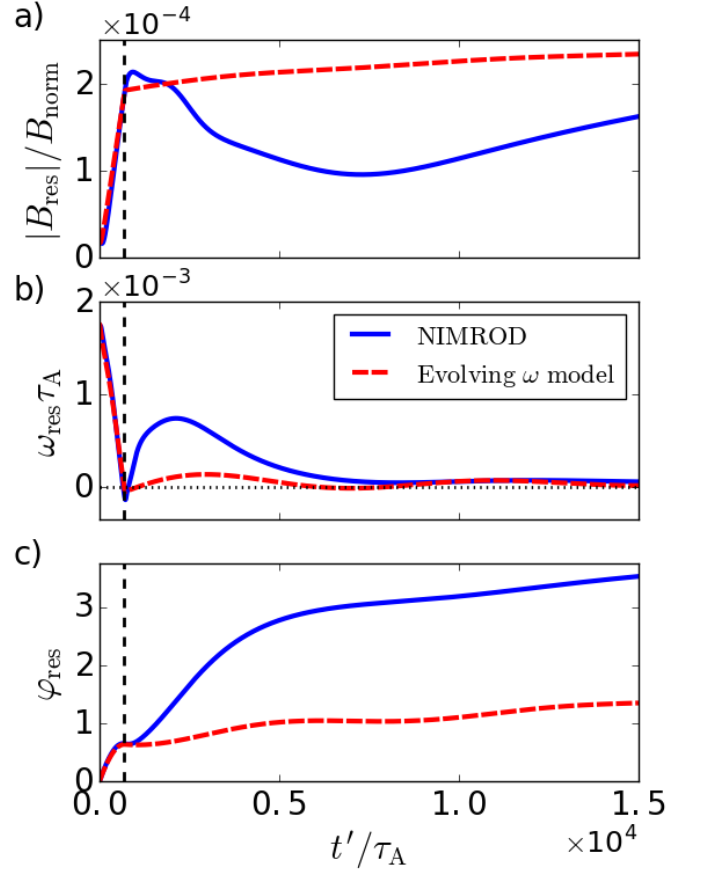


FIG. 12. Comparison between NIMROD results in the solid (blue) traces and analytical predictions in the dashed (red) traces for a) the field response $|B_{\text{res}}|$, b) the flow frequency at the resonant surface ω_{res} , and c) the flow frequency phase φ_{res} . While the results are qualitatively similar, there are quantitative differences in the flow frequency evolution that affects the evolution of the field response upon entering the nonlinear Rutherford regime [50] for $t' \gg 2.0 \times 10^2 \tau_A$.

[adapted from Eq. (47) in Ref. [16]]

$$\frac{dw}{dt} = \bar{D}_\eta \left[a\Delta'_0 + a\Delta'_{\text{ext}} \frac{w_{\text{vac}}^2}{w^2} \cos \varphi_B \right]. \quad (35)$$

Parameters in this equation in addition to those already specified are: effective magnetic field diffusivity $\bar{D}_\eta \equiv (0.8227)^{-1} \eta / \mu_0 = 3.52 \times 10^{-7} D_{\text{norm}} = 0.243 \text{ m}^2/\text{s}$ and the “vacuum” island width that would be produced if $B_{\text{ext},0}$ fully penetrated to the resonant surface is $w_{\text{vac}}/2\delta_{\text{VR}} \simeq 8.33$, which yields $w_{\text{vac}} = 0.124$ m. Additionally, the $V_y \rightarrow 0$ assumption implies the island is in phase with the externally applied field and $\cos \varphi_B \rightarrow 1$.

The equilibrium island width caused by $B_{\text{ext},0}$ is obtained by setting $dw/dt = 0$ in Eq. (35):

$$w_{\text{eq}} = w_{\text{vac}} \left[\frac{\Delta'_{\text{ext}}}{|\Delta'_0|} \right]^{1/2} \simeq 3.6 \times 10^{-2} \text{ m}, \quad (36)$$

for which $B_{\text{res,eq}} \simeq 2.6 \times 10^{-4} B_{\text{norm}}$ and $w_{\text{eq}}/2\delta_{\text{VR}} \gg 1$. These $B_{\text{res,eq}}$ and $w/2\delta_{\text{VR}}$ predictions agree well with the NIMROD results shown in Fig. 2.

A perturbation analysis can be used to determine the ultimate evolution of the island width toward the equi-

librium island width w_{eq} defined in Eq. (36). Here, $w \equiv w_{\text{eq}} + \delta w$ is used and the solution of the perturbed version of Eq. (35) at a time t after an initial difference of $\delta w_0 \equiv w(0) - w_{\text{eq}}$ becomes $\delta w(t) = \delta w_0 e^{-t/\tau_{\text{eq}}}$, in which

$$\tau_{\text{eq}} \equiv \frac{w_{\text{eq}}^3}{2 D_{\eta} \Delta'_{\text{ext}} w_{\text{vac}}^2}. \quad (37)$$

Thus, the island width ultimately approaches its equilibrium value exponentially on the τ_{eq} time scale. For the equilibrium island width in Eq. (36) $\tau_{\text{eq}} \simeq 8.2 \times 10^3 \tau_A = 1.2 \times 10^{-2}$ s. The rate of damping of w agrees reasonably well with the NIMROD results shown in Fig. 2.

Since the island width is caused by the magnitude of the resonant magnetic field perturbation at the resonant surface, its equation is given by

$$|B_{\text{res}}(t)| \equiv \frac{B_{0,z}}{16} \frac{k_y}{L_{\text{sh}}} w(t)^2 = \frac{k_y B_{\text{norm}}}{16} w(t)^2. \quad (38)$$

In the Rutherford regime B_{res} responds twice as fast as w : it approaches its equilibrium value exponentially as $e^{-t/(\tau_{\text{eq}}/2)}$, which is visible in Fig. 2.

In addition, a possible resolution of the differences between the analytic-based model and NIMROD ω_{res} calculations discussed in the preceding subsection could be due to entering the nonlinear Rutherford regime. As discussed previously, this occurs in the NIMROD standard case when $t' \gg 2.0 \times 10^2 \tau_A = 3 \times 10^{-4}$ s. To obtain an evolution equation for ω_{res} analogous to Eq. (34), we would need to perform a matched-asymptotic analysis of Eq. (18) across the magnetic island geometry, similar to that done to determine a MRE in a low-aspect ratio tokamak carried out in [54]. This is beyond the scope of this paper. However, such analysis would increase the inertia term on the left of Eq. (34) by a factor proportional to w/δ_{VR} , require the flow V_{res} jump condition to be evaluated at positions outside the island, and also take account of the growing island-induced eddy currents that could change the resonant frequency and phase of the island relative to the externally applied RMP.

VI. CONCLUSIONS AND DISCUSSION

A. Conclusions

In this work, we show that a transient MHD perturbation applied to an initially high-slip, RMP flow-screened, metastable equilibrium can precipitate mode penetration, which is the transition to a low-slip, field-penetrated, metastable equilibrium. This is modeled using the NIMROD code by starting from an initial configuration that contains a shielded magnetic perturbation that in steady state resides in a high-slip metastable equilibrium. A transient magnetic perturbation is subsequently added that is parameterized by its magnitude, duration, and shape. Depending upon the strength of these parameters, the transient can induce a transition to a low-slip, penetrated resonant magnetic field, producing a large magnetic island. The existence of a metastable

equilibrium consistent with Eq. (12) is essential, in addition to having the background RMP in the metastable region specified by Eqs. (13) and (14). In the absence of metastability, the system will always return to the initial state following a transient perturbation.

NIMROD computations show that the effect of the transient perturbation is to cause the flow frequency to decrease locally at the resonant surface (*e.g.* Fig. 4), which causes additional resonant magnetic field response. Depending on the evolution of the field and flow frequency response due to the transient perturbation, mode penetration to a low-slip state or a return to a high slip state occurs. Furthermore, we observe that the threshold for mode penetration is sensitive to the magnitude, duration, and shape of the transient perturbation as seen in Figs. 6, 7, and 8, respectively. The sensitivity to the shape of the transient perturbation indicates that the history of the evolution is an important feature of mode penetration.

We derive analytic models to predict the evolution of the magnetic field response and flow profile due to a transient perturbation. An approximate model assumes that the EM force is independent of the flow frequency evolution, allowing for a solution using a Green function. It yields an explicit threshold condition for mode penetration given in Eq. (26). A more complete derivation yields expressions that are used to formulate time-dependent EM and viscous forces, which, when balanced with inertia, yield an evolution equation for the flow frequency at the resonant surface. The evolution of the local flow frequency given in Eq. (34) self-consistently determines the evolution of the field response, ultimately governing whether a transient perturbation precipitates mode penetration. Both models qualitatively agree with the presented computational results during the transient as shown in Fig. 11. Evolution of the nonlinear magnetic island resulting from mode penetration also agrees well with predictions of a nonlinear modified Rutherford equation given in Eq. (35).

Comparisons between computational and analytical results give insight into qualitative aspects of flow frequency evolution and mode penetration due to transient perturbations. However, the several approximations entering through linear asymptotic matching procedures needed to derive the EM and viscous forces introduce errors, leading to imperfect quantitative comparisons with computations. Because an analytical treatment that transitions from a linear to a nonlinear asymptotic matching procedure is yet to be developed, we conclude that nonlinear numerical codes such as NIMROD should be employed to accurately determine specific characteristics of mode penetration.

B. Discussion

Experimental observations suggest that the effects of transient MHD events are important for precipitating the transition to an ELM suppressed operating scenarios using RMPs [12]. Furthermore, recent experimental results in DIII-D [55] show a difficulty obtaining ELM suppres-

sion as the input torque is decreased, which is an important operational constraint for ITER. According to Eq. (7), all else being constant, a decrease in the flow is expected to increase the penetrated field. However, if the change in input torque also changes the dissipation parameters altering the linear layer time, the field could be increasingly flow-screened. Additionally, a change in the dissipation parameters would change the condition for the existence of a metastable state according to Eq. (12).

This work shows that a metastable state is required for transient MHD events to precipitate a transition into a low-slip, mode penetrated state. Thus, Eq. (12) effectively sets a flow threshold on the viability of an RMP ELM suppressed operational scenario. The computational and analytical results presented here reinforce this picture. An initial metastable equilibrium and suitable transient perturbation are necessary for mode penetration to occur. Furthermore, to robustly observe the mode penetration threshold, the condition in Eq. (12) needs to be well-exceeded.

While the transient response physics elucidated in this study is directly applicable to the effects of a transient MHD event on the RMP suppression of ELMs, the dynamics of mode penetration due to transient MHD events are also applicable for the triggering of NTMs. Separate experimental work in DIII-D [56, 57] has focused on this issue, capturing well-resolved, high-fidelity measurements of the flow and field evolution during the onset of a $m/n = 2/1$ NTM, with seeding by both ELMs and sawteeth. Aspects of the modeling contained with this work is presently being applied to the analysis of these experiments.

The present visco-resistive, slab geometry model will need to be extended in several aspects to be tokamak relevant. First, it must properly take account of the multi-harmonic coupling between rational surfaces with associated asymptotic matching to link behavior at the coupled surfaces [52]. Second, the accurate evolution of flow in tokamak geometry must self-consistently include poloidal flow damping (*e.g.* Ref. [58]), flow-shear, and differential flow between resonant surfaces. And lastly, to be tokamak relevant this FMR model must be tested with finite β , two-fluid effects [59], and include the role of magnetic flutter (*e.g.* Ref. [60]).

Data used to generate figures can be obtained in digital format by following the link in Ref. [61].

ACKNOWLEDGMENTS

The first author would like to thank K. Bunkers and B. Cornille for helpful discussion related to computations with NIMROD and analysis and visualization with Python.

This research was supported in part by the U. S. Department of Energy (DOE), Office of Science, Office of Fusion Energy Sciences under grants DE-FG02-92ER54139 and DE-FG02-86ER53218. The first author was also supported in part by the U. S. DOE Fusion Energy Sciences Postdoctoral Research Program administered by the Oak Ridge Institute for Science and Ed-

ucation (ORISE) for the DOE. ORISE is managed by Oak Ridge Associated Universities (ORAU) under DOE contract number DE-SC0014664. All opinions expressed in this paper are the authors' and do not necessarily reflect the policies and views of DOE, ORAU, or ORISE. This research used resources of the National Energy Research Scientific Computing Center, a DOE Office of Science User Facility supported by the Office of Science of the U.S. Department of Energy under Contract No. DE-AC02-05CH11231.

Appendix A: Derivation Of Flow Response Using Radially-Localized Green Function

Near the resonant surface Eq. (18) can be solved for the change in flow $\Delta V_y \equiv V_y(x, t') - V_{\text{res}}(0)$ induced by the $\bar{F}_{EM}^{\varphi < 1}$ in Eq. (19) using an infinite medium Green function $G(x, t'|x_0, t_0) = e^{-(x-x_0)^2/4\nu_0(t'-t_0)}/\sqrt{4\pi\nu_0(t'-t_0)}$ which solves $(\partial/\partial t' - \nu_0\partial^2/\partial x^2)G = \delta[x-x_0]\delta[t'-t_0]$:

$$\begin{aligned} \frac{\Delta V_y(x, t')}{V_{\text{res}}(0)} &= \int_0^{t'} dt_0 \int_{-\infty}^{\infty} dx_0 G(x, t'|x_0, t_0) \frac{\bar{F}_{EM}^{\varphi < 1}}{\rho V_{\text{res}}(0)} \\ &= -C_V \int_0^{t'} \frac{ds}{\tau_\mu/a} \frac{e^{-x^2/[4\nu_0(t'-s)]}}{\sqrt{4\pi\nu_0(t'-s)}} \left\{ [\omega_{\text{res}}(0)s]^2 + \frac{2B_{\text{ext},0}}{B_{\text{ext},\text{tot}}} \right\}, \end{aligned}$$

in which $C_V \equiv \frac{[V_{\text{res}}(0)\tau_\mu/a]T\mathcal{E}}{4(k_y a)[\omega_{\text{res}}(0)\tau_{\text{VR}}]} = \frac{(\tau_\mu/\tau_{\text{VR}})T\mathcal{E}}{4(k_y a)^2}$. (A1)

Here, $\tau_\mu \equiv a^2/\nu_0$ and the dimensionless temporal evolution integral in this equation is worked out as follows:

$$\begin{aligned} I_V &\equiv \int_0^{t'} \frac{ds}{\tau_\mu/a} \frac{e^{-x^2/[4\nu_0(t'-s)]}}{\sqrt{4\pi\nu_0(t'-s)}} \left\{ [\omega_{\text{res}}(0)s]^2 + \frac{2B_{\text{ext},0}}{B_{\text{ext},\text{tot}}} \right\} \\ &= \frac{1}{\sqrt{4\pi}} \int_0^{t'/\tau_\mu} \frac{d\hat{t}}{\sqrt{\hat{t}}} \frac{e^{-\hat{x}^2/4\hat{t}}}{\sqrt{\hat{t}}} \left\{ [\omega_{\text{res}}(0)(t' - \tau_\mu\hat{t})]^2 + \frac{2B_{\text{ext},0}}{B_{\text{ext},\text{tot}}} \right\} \\ &= \frac{\sqrt{(t'/\tau_\mu)\epsilon}}{2\sqrt{\pi}} \int_\epsilon^\infty \frac{dz}{z^{3/2}} \frac{e^{-z}}{z^{3/2}} \left\{ [\omega_{\text{res}}(0)t']^2 \left(1 - \frac{2\epsilon}{z} + \frac{\epsilon^2}{z^2} \right) + \frac{2B_{\text{ext},0}}{B_{\text{ext},\text{tot}}} \right\} \\ &= \frac{\sqrt{t'/\tau_\mu}}{2\sqrt{\pi}} \left\{ [\omega_{\text{res}}(0)t']^2 (I_{3/2} - 2\epsilon I_{5/2} + \epsilon^2 I_{7/2}) + \frac{2B_{\text{ext},0}}{B_{\text{ext},\text{tot}}} I_{3/2} \right\}. \end{aligned}$$
 (A2)

Successive lines of this equation for I_V use: first to second line $\hat{t} \equiv (t'-s)/\tau_\mu$, $ds = -\tau_\mu d\hat{t}$, $s = t' - \tau_\mu\hat{t}$ and $\hat{x} \equiv x/a$; and second to third line $z \equiv \hat{x}^2/4\hat{t}$, $\hat{t} = \hat{x}^2/4z$, $d\hat{t} = -(\hat{x}^2/4z^2) dz$ and $\epsilon^{1/2} \equiv |\hat{x}|/\sqrt{4t'/\tau_\mu}$. The fourth line makes use of the dimensionless integrals

$$I_\alpha \equiv \sqrt{\epsilon} \int_\epsilon^\infty dz \frac{e^{-z}}{z^\alpha} = -\frac{\sqrt{\epsilon}}{\alpha-1} \left[\frac{e^{-z}}{z^{\alpha-1}} \Big|_\epsilon^\infty + \int_\epsilon^\infty dz \frac{e^{-z}}{z^{\alpha-1}} \right]. \quad (\text{A3})$$

The second form of this integral is obtained via integration by parts in the form $\int u dv = uv - \int v du$. Identifying the variables as $u = e^{-z}$ and $v \equiv -[1/(\alpha-1)](1/z^{\alpha-1})$ so $dv = dz/z^\alpha = -[1/(\alpha-1)]d(1/z^{\alpha-1})$ yields the general $\alpha > 1$ result indicated. The fundamental integral is

$I_{3/2}$ which for $\sqrt{\epsilon} \ll 1$ is

$$\begin{aligned} I_{3/2} &\equiv \sqrt{\epsilon} \int_{\epsilon}^{\infty} dz \frac{e^{-z}}{z^{3/2}} = -2\sqrt{\epsilon} \left[\frac{e^{-z}}{z^{1/2}} \Big|_{\epsilon}^{\infty} + \int_{\epsilon}^{\infty} dz \frac{e^{-z}}{z^{1/2}} \right] \\ &= 2e^{-\epsilon} - 2\sqrt{\pi\epsilon} \operatorname{erfc}(\sqrt{\epsilon}) \\ &\simeq 2 - 2\sqrt{\pi\epsilon} + 2\epsilon + \mathcal{O}\{\epsilon^{3/2}\}. \end{aligned} \quad (\text{A4})$$

Here, $z \equiv y^2$ and $dz = 2y dy$ have been used to show that $\int_{\epsilon}^{\infty} dz e^{-z}/z^{1/2} = 2 \int_{\sqrt{\epsilon}}^{\infty} dy e^{-y^2} = \sqrt{\pi} \operatorname{erfc}(\sqrt{\epsilon})$, in which $\operatorname{erfc}(x) \equiv (2/\sqrt{\pi}) \int_x^{\infty} dy e^{-y^2} \simeq 1 - 2x/\sqrt{\pi} + \mathcal{O}\{x^3\}$ is the complimentary error function. The $I_{5/2}$ and $I_{7/2}$ integrals can be related to $I_{3/2}$ using Eq. (A3).

Combining the results in Eqs. (A2), (A4) and (A3), and using them in Eq. (A1) yields

$$\begin{aligned} \frac{\Delta V_y(x, t')}{V_{\text{res}}(0)} &= -\frac{C_V/(2\sqrt{\pi})}{[\omega_{\text{res}}(0)\tau_{\mu}]^{1/2}} f_V(x, t'), \text{ in which} \\ f_V(x, t') &\equiv [\omega_{\text{res}}(0)t']^{1/2} \left\{ \frac{16}{15} [\omega_{\text{res}}(0)t']^2 F_{VT} + \frac{4B_{\text{ext},0}}{B_{\text{ext,tot}}} F_{V0} \right\}. \end{aligned} \quad (\text{A5})$$

For $\sqrt{\epsilon} \ll 1$ the dimensionless spatial variation functions in $f_V(x, t')$ obtained using Eqs. (A3) and (A4) in the last line of Eq. (A2) are

$$\begin{aligned} F_{VT}[x, L_V(t)] &\equiv \frac{15}{16} \sqrt{\epsilon} \int_{\epsilon}^{\infty} dz e^{-z} \left(\frac{1}{z^{3/2}} - \frac{2\epsilon}{z^{5/2}} + \frac{\epsilon^2}{z^{7/2}} \right) \\ &\simeq 1 - \frac{15}{16} \sqrt{\pi} \frac{|x|}{L_V} + \frac{4}{3} \frac{x^2}{L_V^2} + \mathcal{O} \left\{ \frac{|x|^3}{L_V^3} \right\}, \end{aligned} \quad (\text{A6})$$

$$\begin{aligned} F_{V0}[x, L_V(t)] &\equiv \frac{\sqrt{\epsilon}}{2} \int_{\epsilon}^{\infty} dz e^{-z} \left(\frac{1}{z^{3/2}} \right) \\ &\simeq 1 - \sqrt{\pi} \frac{|x|}{2L_V} + \frac{x^2}{4L_V^2} + \mathcal{O} \left\{ \frac{|x|^3}{L_V^3} \right\}. \end{aligned} \quad (\text{A7})$$

Note that the functions F_{VT} and F_{V0} are both unity at the $x = 0$ resonant surface. The approximate forms of Eqs. (A6) and (A7) are obtained using $\epsilon^{1/2} = |x|/(4\nu_0 t')^{1/2} \equiv |x|/2L_V(t') \ll 1$, in which the reference scale length is $L_V(t') \equiv (\nu_0 t')^{1/2}$.

For the NIMROD standard case at $t' = 345\tau_A \simeq 5 \times 10^{-4} \text{ s}$ $L_V \simeq 0.045 \text{ m}$, while for $t' = 690\tau_A \simeq 10^{-3} \text{ s}$ $L_V \simeq 0.063 \text{ m}$. The spatial functions in Eqs. (A6) and (A7) cause $f_V(x, t')$ to first decay in space linearly with increasing $|x|/L_V$ but for $L_V \lesssim |x| < 2L_V$ decrease more slowly with increasing $|x|/L_V$. This behavior roughly agrees with the spatial variation of the $V_y \equiv V_{\text{res}}(0) + \Delta V_y(x, t)$ profiles shown in the zoomed in part of Fig. 4.

Appendix B: Calculation of Flow Profile by Infinite-Series Eigenfunction Expansion

The general equation for the y -component of the flow evolution is provided by Eq. (18). Outside the infinitesimal layer width δ_{VR} the EM force vanishes, which yields a diffusion equation for the flow profile

$$\frac{\partial V_y(x, t')}{\partial t'} = \frac{\partial}{\partial x} \left[\nu_0 \bar{\nu}(x) \frac{\partial V_y(x, t')}{\partial x} \right]. \quad (\text{B1})$$

Because we expect the flow profile to be even, consistent with Fig. 4, we solve Eq. (B1) in the region $0 \lesssim x < a_{\nu}$. This calculation is simplified by solving for $\Delta V_y(x, t') = V_0 - V_y(x, t')$, yielding no-slip boundary conditions

$$\Delta V_y(x = 0, t') = V_0 - V_{\text{res}}(t') \equiv \Delta V_y(t'), \quad (\text{B2a})$$

$$\Delta V_y(x = a_{\nu}, t') = 0, \quad (\text{B2b})$$

where $V_{\text{res}}(t') = V_y(x = 0, t')$. The initial condition at $t' = 0$ is given by

$$\Delta V_y(x, t' = 0) \equiv \Delta V_y(x), \quad (\text{B3})$$

to treat evolution starting from time-asymptotic equilibria that have a different flow profile than the initial flow V_0 .

Because Eq. (B1) is a linear equation, we can write

$$\Delta V_y(x, t') = U(x, t') + W(x, t'). \quad (\text{B4})$$

By choosing

$$W(x, t') = \Delta V_y(t') \left[1 - \frac{x}{a_{\nu}} \right], \quad (\text{B5})$$

which is equal to the time-asymptotic solution of Eq. (B1), for $0 \lesssim x < a_{\nu}$ Eq. (B1) becomes

$$\frac{\partial \Delta V_y}{\partial t'} = \nu_0 \frac{\partial^2 \Delta V_y}{\partial x^2} \Rightarrow \frac{\partial U}{\partial t'} = \nu_0 \frac{\partial^2 U}{\partial x^2} - \underbrace{\frac{d\Delta V_y(t')}{dt'}}_{+S(x, t')} \left[1 - \frac{x}{a_{\nu}} \right], \quad (\text{B6})$$

where we effectively converted a PDE with a time-dependent boundary, to a PDE with a source $S(x, t')$. The boundary conditions for Eq. (B6) are

$$U(x = 0, t') = U(x = a_{\nu}, t') = 0, \quad (\text{B7})$$

and the initial condition is

$$U(x, t' = 0) = \Delta V_y(x) - \Delta V_y(0) \left[1 - \frac{x}{a_{\nu}} \right], \quad (\text{B8})$$

where $\Delta V_y(0) \equiv \Delta V_y(x = 0, t' = 0)$. Note that if $\Delta V_y(x)$ is consistent with a time-asymptotic state, $U(x, 0) = 0$.

Next, because of the homogeneous boundary conditions on u , we use an eigenfunction expansion for u of the form

$$U(x, t') = \sum_{n=1}^{\infty} \hat{U}_n(t') \sin \left(\frac{n\pi x}{a_{\nu}} \right). \quad (\text{B9})$$

Using a similar expansion, the source becomes

$$S(x, t') = \sum_{n=1}^{\infty} \hat{S}_n(t') \sin \left(\frac{n\pi x}{a_{\nu}} \right), \quad (\text{B10})$$

and orthogonality of the separate n terms allows us to write

$$\begin{aligned} \hat{S}_n(t') &= \frac{2}{a_{\nu}} \int_0^{a_{\nu}} dx \sin \left(\frac{n\pi x}{a_{\nu}} \right) \left\{ -\frac{d\Delta V_y(t')}{dt'} \left[1 - \frac{x}{a_{\nu}} \right] \right\} \\ &= -\frac{2}{n\pi} \frac{d\Delta V_y(t')}{dt'}. \end{aligned} \quad (\text{B11})$$

Taking derivatives of Eq. (B9) and inserting into Eq. (B6) with Eqs. (B10) and (B11) yields

$$0 = \sum_{n=1}^{\infty} \left[\frac{\partial \hat{U}_n(t')}{\partial t'} + \nu_0 \left(\frac{n\pi}{a_\nu} \right)^2 \hat{U}_n(t') - \hat{S}_n(t') \right] \sin \left(\frac{n\pi x}{a_\nu} \right). \quad (\text{B12})$$

Because terms for different n are orthogonal, the factor in the brackets must be equal to 0 for all n . This equation can be solved using an integration factor, which yields

$$\frac{d}{dt'} \left[e^{(n\pi)^2 \frac{t'}{\tau_\nu}} \hat{U}_n(t') \right] = -\frac{2}{n\pi} \frac{d\Delta V_y(t')}{dt'} e^{(n\pi)^2 \frac{t'}{\tau_\nu}}, \quad (\text{B13})$$

where $\tau_\nu = a_\nu^2/\nu_0$ is the global viscous time with a nonuniform viscosity profile. Integrating and rearranging Eq. (B13) yields

$$\hat{U}_n(t') = \hat{U}_n(0) e^{-(n\pi)^2 \frac{t'}{\tau_\nu}} - \frac{2}{n\pi} \int_0^{t'} ds \frac{d\Delta V_y(s)}{ds} e^{-(n\pi)^2 \frac{t'-s}{\tau_\nu}}. \quad (\text{B14})$$

To find $\hat{u}_n(0)$, utilize the initial condition in Eq. (B9)

and orthogonality to yield

$$\hat{U}_n(0) = \frac{2}{a_\nu} \int_0^{a_\nu} dx \sin \left(\frac{n\pi x}{a_\nu} \right) \times \left\{ \Delta V_y(x) - \Delta V_y(0) \left[1 - \frac{x}{a_\nu} \right] \right\}. \quad (\text{B15})$$

Putting together Eqs. (B4), (B5), (B9), (B14), and (B15), and writing in terms of $V_y(x, t')$ yields

$$\begin{aligned} V_y(x, t') &= V_{\text{res}}(t') + [V_0 - V_{\text{res}}(t')] \left(\frac{x}{a_\nu} \right) \\ &- \sum_{n=1}^{\infty} \sin \left(\frac{n\pi x}{a_\nu} \right) e^{-(n\pi)^2 \frac{t'}{\tau_\nu}} \left\{ \frac{2}{a_\nu} \int_0^{a_\nu} dx \sin \left(\frac{n\pi x}{a_\nu} \right) \right. \\ &\times \left[V_y(x) - \left\{ V_{\text{res}}(0) + [V_0 - V_{\text{res}}(0)] \left(\frac{x}{a_\nu} \right) \right\} \right] \\ &\left. + \frac{2}{n\pi} \int_0^{t'} ds \frac{dV_{\text{res}}(s)}{ds} e^{(n\pi)^2 \frac{s}{\tau_\nu}} \right\}. \quad (\text{B16}) \end{aligned}$$

The first term is the time-asymptotic flow profile, while the two terms in the infinite sum correspond to components of the flow profile viscously damped from the initial flow profile and the time rate of change of the flow at the resonant surface.

-
- [1] R. J. L. Haye, *Physics of Plasmas* **13**, 055501 (2006).
- [2] R. Nazikian, C. Paz-Soldan, J. D. Callen, J. S. deGrassie, D. Eldon, T. E. Evans, N. M. Ferraro, B. A. Grierson, R. J. Groebner, S. R. Haskey, et al., *Phys. Rev. Lett.* **114**, 105002 (2015).
- [3] C. Paz-Soldan, R. Nazikian, S. R. Haskey, N. C. Logan, E. J. Strait, N. M. Ferraro, J. M. Hanson, J. D. King, M. J. Lanctot, R. A. Moyer, et al., *Phys. Rev. Lett.* **114**, 105001 (2015).
- [4] M. T. Beidler, J. D. Callen, C. C. Hegna, and C. R. Sovinec, *Phys. Plasmas* **24**, 052508 (2017), erratum: *ibid.* **25**, 049901 (2018).
- [5] P. de Vries, M. Johnson, B. Alper, P. Buratti, T. Hender, H. Koslowski, V. Riccardo, and J.-E. Contributors, *Nucl. Fusion* **51**, 053018 (2011).
- [6] A. Loarte, G. Saibene, R. Sartori, D. Campbell, M. Becoulet, L. Horton, T. Eich, A. Herrmann, G. Matthews, N. Asakura, et al., *Plasma Phys. and Control. Fusion* **45**, 1549 (2003).
- [7] T. C. Hender, J. C. Wesley, J. Bialek, A. Bondeson, A. H. Boozer, R. J. Buttery, A. Garofalo, T. P. Goodman, R. S. Granetz, Y. Gribov, et al., *Nucl. Fusion* **47**, S128 (2007).
- [8] T. E. Evans, R. A. Moyer, P. R. Thomas, J. G. Watkins, T. H. Osborne, J. A. Boedo, E. J. Doyle, M. E. Fenstermacher, K. H. Finken, R. J. Groebner, et al., *Phys. Rev. Lett.* **92**, 235003 (2004).
- [9] R. A. Moyer, T. E. Evans, T. H. Osborne, P. R. Thomas, M. Becoulet, J. Harris, K.-H. Finken, J. A. Boedo, E. J. Doyle, M. E. Fenstermacher, et al., *Phys. Plasmas* **12**, 056119 (2005).
- [10] T. E. Evans, R. A. Moyer, K. H. Burrell, M. E. Fenstermacher, I. Joseph, A. W. Leonard, T. H. Osborne, G. D. Porter, M. J. Schaffer, P. B. Snyder, et al., *Nature Phys.* **2**, 419 (2006).
- [11] T. Evans, M. Fenstermacher, R. Moyer, T. Osborne, J. Watkins, P. Gohil, I. Joseph, M. Schaffer, L. Baylor, M. Becoulet, et al., *Nucl. Fusion* **48**, 024002 (2008).
- [12] J. D. Callen, R. Nazikian, C. Paz-Soldan, N. M. Ferraro, M. T. Beidler, C. C. Hegna, and R. J. L. Haye, report UW-CPTC 16-4, Dec. 20, 2016 (to be published).
- [13] T. S. Hahm and R. M. Kulsrud, *Phys. Fluids* **28**, 2412 (1985).
- [14] R. Fitzpatrick and T. C. Hender, *Phys. Fluids B* **3**, 644 (1991).
- [15] R. Fitzpatrick, *Nucl. Fusion* **33**, 1049 (1993).
- [16] R. Fitzpatrick, *Phys. Plasmas* **5**, 3325 (1998).
- [17] Y. Kikuchi, M. F. M. de Bock, K. H. Finken, M. Jakubowski, R. Jaspers, H. R. Koslowski, A. Kraemer-Flecken, M. Lehnen, Y. Liang, G. Matsunaga, et al. (TEXTOR-team), *Phys. Rev. Lett.* **97**, 085003 (2006).
- [18] J.-K. Park, A. H. Boozer, and A. H. Glasser, *Phys. Plasmas* **14**, 052110 (2007).
- [19] M. F. Heyn, I. B. Ivanov, S. V. Kasilov, W. Kernbichler, I. Joseph, R. A. Moyer, and A. M. Runov, *Nucl. Fusion* **48**, 024005 (2008).
- [20] Q. Yu, S. Günter, Y. Kikuchi, and K. Finken, *Nucl. Fusion* **48**, 024007 (2008).
- [21] V. Izzo and I. Joseph, *Nucl. Fusion* **48**, 115004 (2008).
- [22] H. Strauss, L. Sugiyama, G. Park, C. Chang, S. Ku, and I. Joseph, *Nucl. Fusion* **49**, 055025 (2009).
- [23] E. Nardon, P. Tamain, M. Becoulet, G. Huysmans, and F. Waelbroeck, *Nucl. Fusion* **50**, 034002 (2010).
- [24] Y. Liu, A. Kirk, and E. Nardon, *Phys. Plasmas* **17**, 122502 (2010).
- [25] Q. Yu and S. Günter, *Nucl. Fusion* **51**, 073030 (2011).
- [26] N. M. Ferraro, *Phys. Plasmas* **19**, 056105 (2012).
- [27] Y. Q. Liu, A. Kirk, Y. Sun, P. Cahyna, I. T. Chapman,

- P. Denner, G. Fishpool, A. M. Garofalo, J. R. Harrison, E. Nardon, et al., *Plasma Phys. and Conrol. Fusion* **54**, 124013 (2012).
- [28] N. Ferraro, T. Evans, L. Lao, R. Moyer, R. Nazikian, D. Orlov, M. Shafer, E. Unterberg, M. Wade, and A. Wingen, *Nucl. Fusion* **53**, 073042 (2013).
- [29] F. Orain, M. Bécoulet, G. Dif-Pradalier, G. Huijsmans, S. Pamela, E. Nardon, C. Passeron, G. Latu, V. Grandgirard, A. Fil, et al., *Phys. Plasmas* **20**, 102510 (2013).
- [30] S. R. Haskey, M. J. Lanctot, Y. Q. Liu, J. M. Hanson, B. D. Blackwell, and R. Nazikian, *Plasma Phys. and Conrol. Fusion* **56**, 035005 (2014).
- [31] M. Bécoulet, F. Orain, G. T. A. Huijsmans, S. Pamela, P. Cahyna, M. Hoelzl, X. Garbet, E. Franck, E. Sonnendrücker, G. Dif-Pradalier, et al., *Phys. Rev. Lett.* **113**, 115001 (2014).
- [32] S. R. Haskey, M. J. Lanctot, Y. Q. Liu, C. Paz-Soldan, J. D. King, B. D. Blackwell, and O. Schmitz, *Plasma Phys. and Conrol. Fusion* **57**, 025015 (2015).
- [33] Y. Liu, R. Akers, I. Chapman, Y. Gribov, G. Hao, G. Huijsmans, A. Kirk, A. Loarte, S. Pinches, M. Reinke, et al., *Nucl. Fusion* **55**, 063027 (2015).
- [34] F. Orain, M. Bécoulet, J. Morales, G. T. A. Huijsmans, G. Dif-Pradalier, M. Hoelzl, X. Garbet, S. Pamela, E. Nardon, C. Passeron, et al., *Plasma Phys. and Conrol. Fusion* **57**, 014020 (2015).
- [35] J. Kim, S. S. Kim, and H. Jhang, *Phys. Plasmas* **23**, 092502 (2016).
- [36] T. Markovic, Y. Liu, P. Cahyna, R. Pánek, M. Peterka, M. Aftanas, P. Bílková, P. Bohm, M. Imříšek, P. Háček, et al., *Nucl. Fusion* **56**, 092010 (2016).
- [37] F. Orain, M. Hölzl, E. Viezzer, M. Dunne, M. Bécoulet, P. Cahyna, G. Huijsmans, J. Morales, M. Willensdorfer, W. Suttrop, et al., *Nucl. Fusion* **57**, 022013 (2017).
- [38] N. Ivanov and A. Kakurin, *Nucl. Fusion* **57**, 016021 (2017).
- [39] N. V. Ivanov and A. M. Kakurin, *Phys. Plasmas* **21**, 102502 (2014).
- [40] S. Inoue, J. Shiraishi, M. Takechi, G. Matsunaga, A. Isayama, N. Hayashi, and S. Ide, *Nucl. Fusion* **57**, 116020 (2017).
- [41] C. C. Hegna, J. D. Callen, and R. J. LaHaye, *Phys. Plasmas* **6**, 130 (1999).
- [42] V. Igochine, A. Gude, S. Günter, K. Lackner, Q. Yu, L. B. Orte, A. Bogomolov, I. Classen, R. M. McDermott, N. C. L. Jr., et al., *Phys. Plasmas* **21**, 110702 (2014), <https://doi.org/10.1063/1.4902106>, URL <https://doi.org/10.1063/1.4902106>.
- [43] V. Igochine, I. Classen, M. Dunne, A. Gude, S. Günter, K. Lackner, R. McDermott, M. Sertoli, D. Vezinet, M. Willensdorfer, et al., *Nucl. Fusion* **57**, 036015 (2017).
- [44] C. Sovinec, A. Glasser, T. Gianakon, D. Barnes, R. Nebel, S. Kruger, D. Schnack, S. Plimpton, A. Tarditi, and M. Chu, *J. Comp. Phys.* **195**, 355 (2004).
- [45] C. Sovinec and J. King, *J. Comp. Phys.* **229**, 5803 (2010).
- [46] L. Comisso, D. Grasso, and F. L. Waelbroeck, *Phys. Plasmas* **22**, 042109 (2015).
- [47] H. P. Furth, J. Killeen, and M. N. Rosenbluth, *Phys. Fluids* **6**, 459 (1963).
- [48] R. Fitzpatrick, *Phys. Plasmas* **11**, 937 (2004).
- [49] R. Fitzpatrick, *Phys. Plasmas* **11**, 3961 (2004).
- [50] P. H. Rutherford, *Phys. Fluids* **16**, 1903 (1973).
- [51] A. Cole and R. Fitzpatrick, *Phys. Plasmas* **11**, 3525 (2004).
- [52] R. Fitzpatrick, *Phys. Plasmas* **1**, 3308 (1994).
- [53] URL <https://docs.scipy.org/doc/scipy/reference/generated/scipy.integrate.odeint.html>.
- [54] C. C. Hegna, *Phys. Plasmas* **6**, 3980 (1999).
- [55] C. Paz-Soldan, Private Communication (2017).
- [56] R. J. L. Haye, Private Communication (2016).
- [57] N. Z. Taylor, Private Communication (2017).
- [58] P. Helander and D. Sigmar, *Collisional Transport in Magnetized Plasmas* (Cambridge University Press, 2002).
- [59] A. Cole and R. Fitzpatrick, *Phys. Plasmas* **13** (2006).
- [60] J. Callen, C. Hegna, and A. Cole, *Nucl. Fusion* **53**, 113015 (2013).
- [61] URL <https://cptc.wisc.edu/report/>.